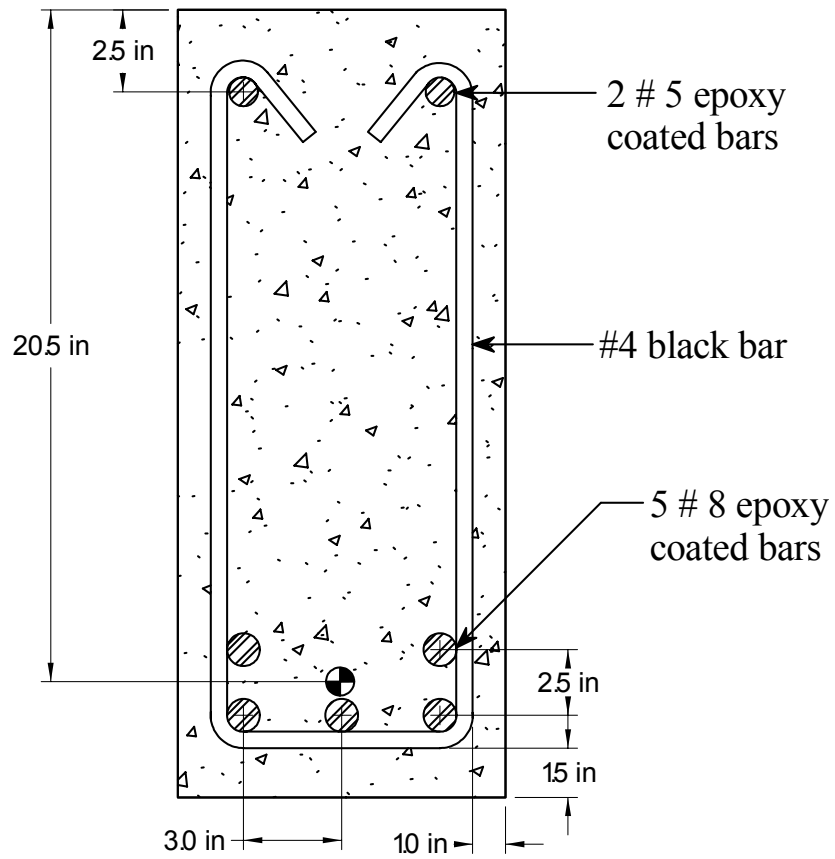


## **APPENDICES**



**Appendix A**  
**Experimental Specimens**



**TYPE I cross-section**

Figure A1: Cross-section of rectangular beam specimen

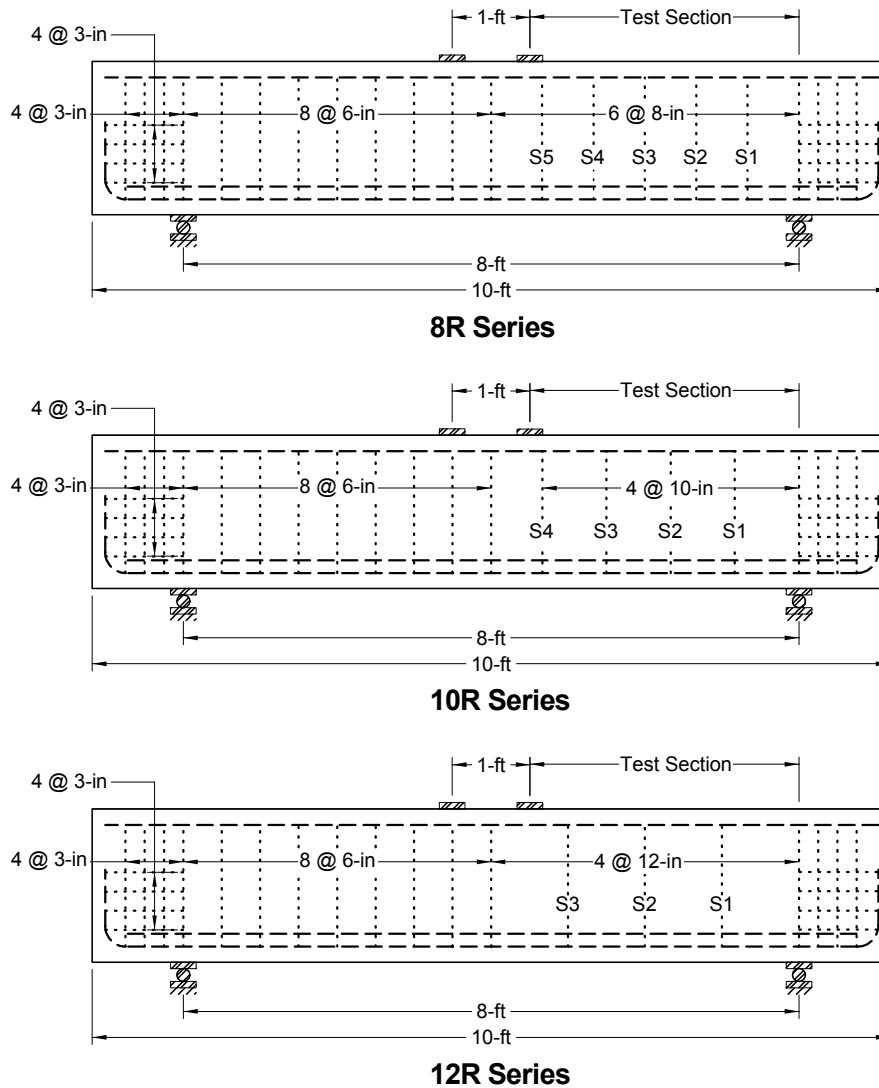
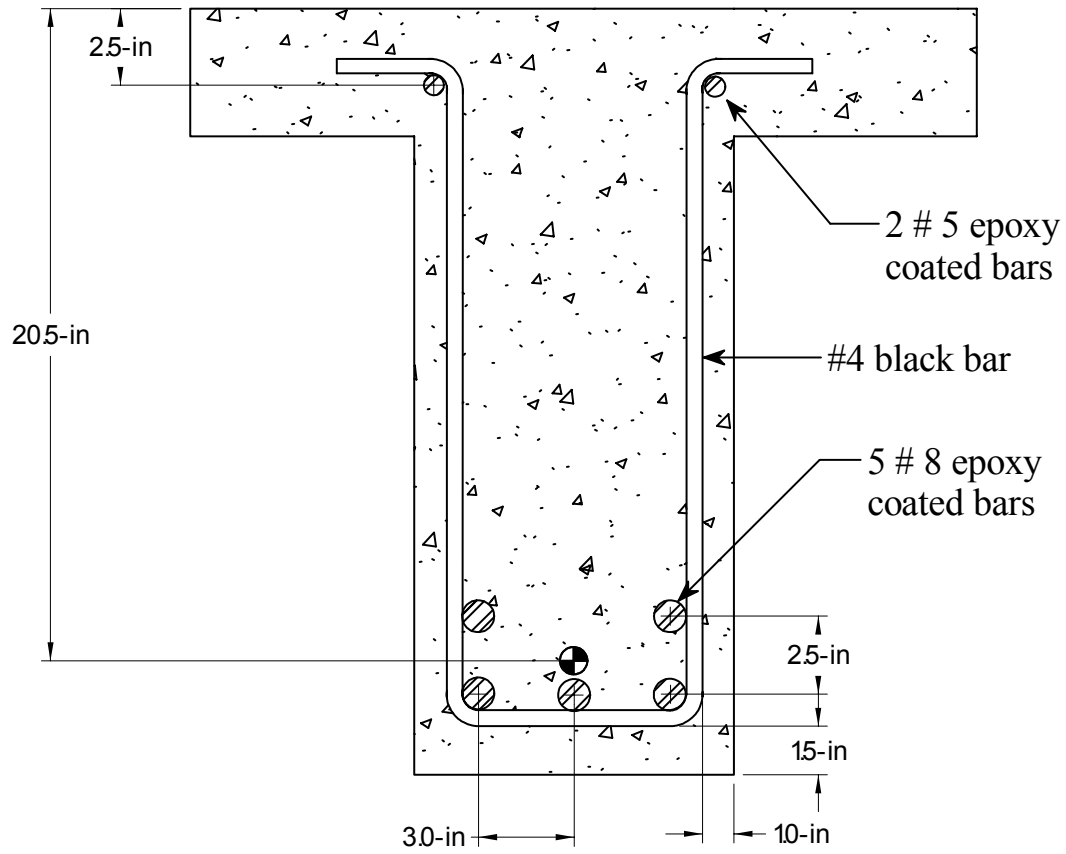


Figure A2: Plan and elevation views of rectangular beam specimens



**TYPE II cross-section**

Figure A3: Cross-section view of T-beam specimens

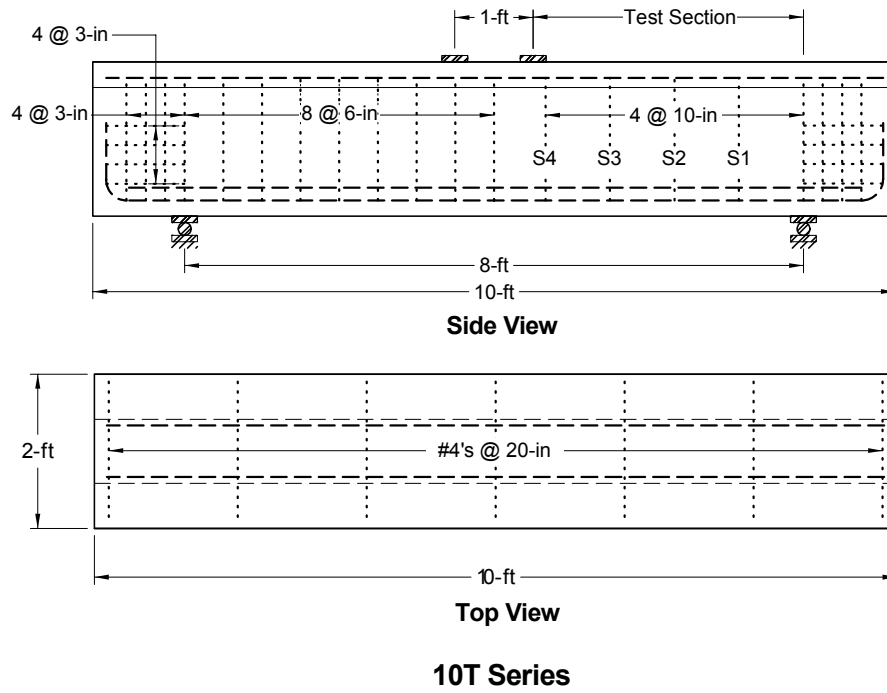
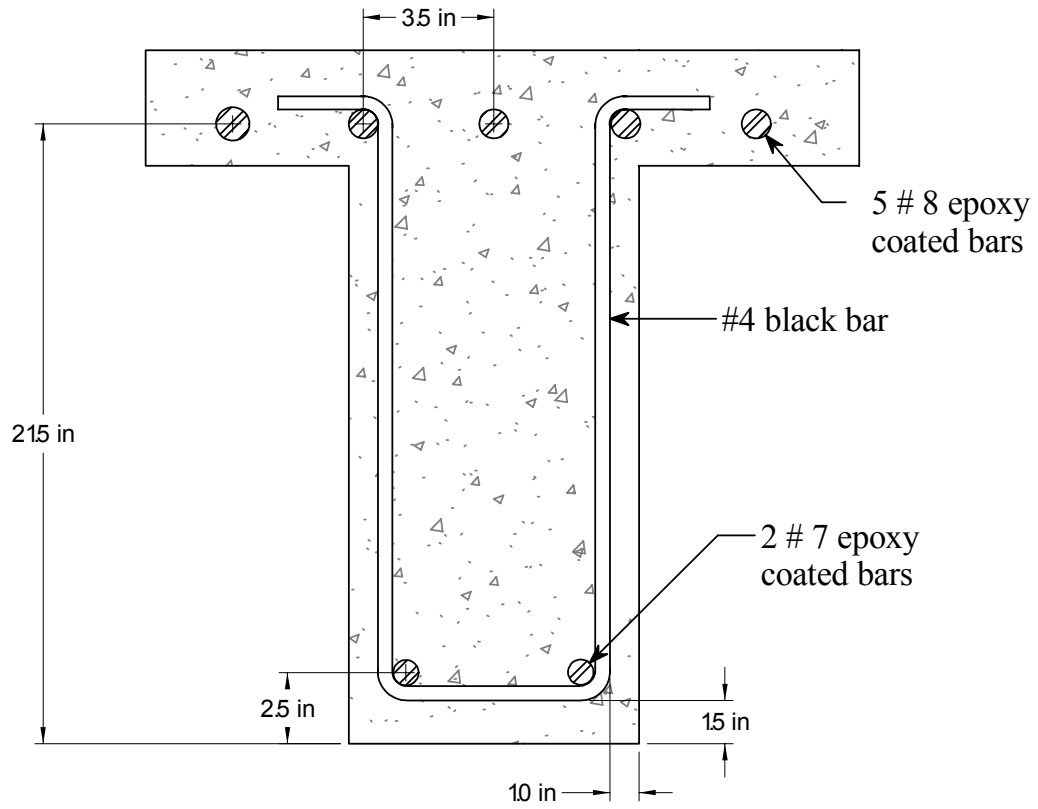


Figure A4: Plan and elevation views of T-beam specimens



**TYPE III Cross-section**

Figure A5: Cross-section view of inverted T-beam specimens

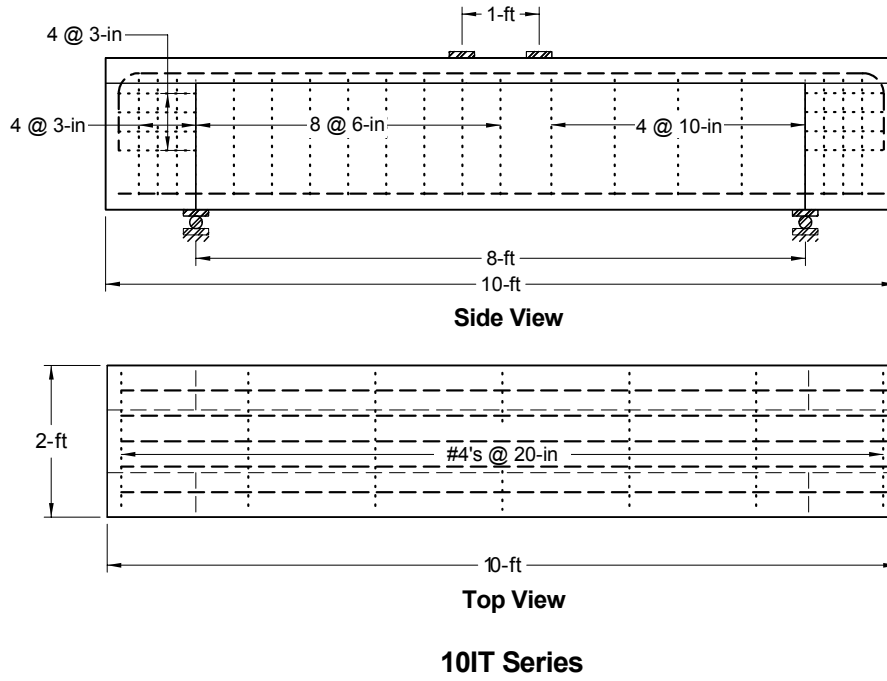


Figure A6: Plan and elevation views of inverted T-beam specimens



**Appendix B**  
**Finite Element Analysis**

# Corrosion Modeling Using Finite Element Method

## Experimental beams

Finite element modeling was employed to investigate effects of corrosion damage on four experimental beams with rectangular section (Type I). The experimental beams were designed to fail in shear and were constructed with 6-inch stirrup spacing on one side and 10-inch stirrup spacing on the other side. This configuration forced failure within the portion of the beam containing 10-inch stirrup spacing. Within each test span there were four corroded stirrups. Four experimental beams exhibiting different corrosion damage states were considered. These were designated specimens: 10RA, 10RB, 10RC, and 10RD. Specimen 10RA had no corrosion damage. Specimens 10RB, 10RC, and 10RD beams had light, moderate, and severe damage states, respectively. Prior to testing, the experimental beams were visually inspected for damage. Concrete cracks due to expansion of corrosion products were observed adjacent to locations of the corroded stirrups and along the top and bottom of the beams along the flexural steel. Delaminations and spalled areas of concrete cover in the test spans were identified as well. Detailed damage data are described in the main report.

After failure, 2 stirrups that crossed the shear failure crack were removed from each beam. Measurements of the remaining cross-sectional areas for the corroded stirrups were made. Both average section-loss along the length and local maximum section-loss were determined for the corroded stirrups. Means of average and local maximum section-losses were 13% and 34%; 23% and 61%; 26% and 100% for 10RB, 10RC, and 10RD beams, respectively. Table B1 shows the cross-sectional areas of the stirrups. The maximum load, deflection at the maximum load, and energy for each of the experimental beams are shown in Table B2. Load-deflection responses for the experimental beams are shown in Figure B1. Experimental results showed the ultimate strengths of specimens 10RB, 10RC, and 10RD were 12%, 19%, and 30% lower, respectively, than the ultimate strength of specimen 10RA. Energy of the beams was also used for comparisons, taken as the area under the load-deflection curve starting from initial loading to the maximum load before unloading. Specimens 10RB, 10RC, and 10RD demonstrated 24%, 47%, and 55% energy reductions, respectively, compared to specimen 10RA.

**Table B1: Average and local maximum cross-sectional losses for experimental stirrup specimens**

Specimen		Average		Local Maximum	
		Area (in <sup>2</sup> )	% Section Loss	Area (in <sup>2</sup> )	% Section Loss
10RB	S2-1	0.1721	14.0	0.1488	25.6
	S2-2	0.1746	12.7	0.1659	17.1
	S3-1	0.1767	11.7	0.1318	<b>34.1</b>
	S3-2	0.1709	14.6	0.1349	32.6
		Mean	<b>13.2</b>		
10RC	S2-1	0.1583	20.9	0.1550	22.5
	S2-2	0.1423	28.9	0.0775	<b>61.3</b>
	S3-1	0.1607	19.7	0.1440	28.0
	S3-2	0.1540	23.0	0.1209	39.6
		Mean	<b>23.1</b>		
10RD	S2-1	0.1250	37.5	0	<b>100.0</b>
	S2-2	0.1123	43.9	0.046	77.0
	S3-1	0.1735	13.3	0.162	19.0
	S3-2	0.1830	8.5	0.158	21.0
		Mean	<b>25.8</b>		

**Table B2: Summary of experimental and finite element modeling results**

Experimental Beam	Maximum Load (kips)	Deflection at Max. Load (inch)	Energy (inch-kips)
10RA	260.4	0.404	66.5
10RB	228.0	0.329	50.6
10RC	210.2	0.286	35.2
10RD	182.7	0.269	30.0
<b>Finite Element Model</b>			
<i>No Spall (Effective width = 10 inches)</i>			
0% As loss (no corrosion damage)	267.5	0.464	80.7
50%As loss	250.1	0.381	57.6
100% As loss	184.2	0.259	27.8
<i>Spall (Effective width = 8 inches)</i>			
0% As loss	238.6	0.349	48.3
50%As loss	231.5	0.335	44.0
100% As loss	179.8	0.271	28.1
<i>Debonded concrete-rebar interface</i>			
0% As loss with spalled cover	206.8	0.309	37.3
50% As loss with spalled cover	206.3	0.326	40.6
SP2 (0% Average, 75% local maximum)	191.8	0.280	31.2
SP2 (50% Average, 75% local maximum)	181.2	0.277	30.1

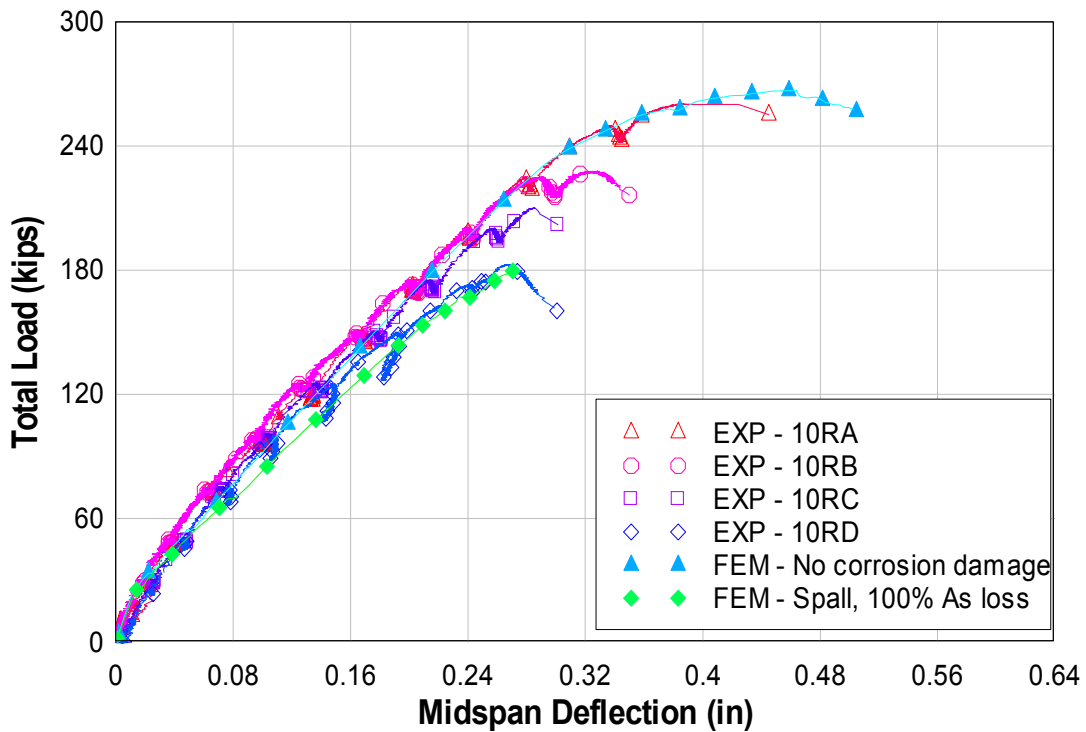


Figure B1: Load-deflection response for experimental results and FE models corresponding to no damage and complete rebar cross-sectional loss with concrete spalling

## Finite element models

Using finite element analysis, corrosion damage components were isolated (i.e. concrete cover spalling, stirrup cross-sectional loss, and debonding at concrete-rebar interfaces). This enabled identification of the contribution of corrosion damage constituents to structural performance deterioration. FE analyses of the beam specimens were performed using ANSYS version 7.0. For the specimens considered, only half of the experimental beam was modeled due to symmetry. Embedded reinforcing steel was modeled using nonlinear truss elements rigidly connected to the surrounding concrete elements. Rebar material properties were determined from tensile tests. Concrete was modeled using 8-node solid elements. Constitutive modeling of the concrete was performed using Todeschini's approximation for the compressive stress-strain relationship [Todeschini et al., 1964], with parameters based on best-fit of actual cylinder compression tests. To account for confining effects at the load application points, concrete elements near midspan were modified to permit slower post-peak decay in compressive stress, at support and loading locations. Analyses were performed using a quasi-displacement control technique whereby high-stiffness springs are used to control the midspan displacement of the model and the resulting forces are computed based on support reactions. The spring stiffness is adjusted through trial and error such that numerical stability of the solution is achieved as the model becomes highly nonlinear at concrete cracking/crushing and rebar yielding without losing precision. Without this technique, solution times become exceedingly large and peak and post-peak response cannot be well captured using current concrete models in ANSYS.

A baseline model without corrosion damage was developed as shown in Figure B2. Only half of the experimental beam was modeled due to symmetry. Results from the finite element analysis are compared with specimen 10RA data. As shown in Figure B1, the load-deflection response of the finite element model with no corrosion damage compares well with experimental response. The ultimate capacity and energy of the FE model were 3% and 21% higher than those of specimen 10RA (Table B2). In addition to the ultimate load and energy comparisons, a "crack pattern" considering maximum principal strains was compared with the crack pattern at failure of the experimental beam. As shown in Figure B3a, the crack patterns are similar. Steel strains in the flexural steel for the undamaged model and specimen 10RA are compared and shown in Figure B4. The flexural rebars in the FE model and specimen 10RA both yielded. The interior lower-layer (LL-I) rebar yielded at a load of 230 kips for the FE model and at a load of 204 kips for specimen 10RA, a 13% difference. The upper-layer (UL) rebar yielded at a load of 255 kips for the model and a load of 233 kips for specimen 10RA, a 9% difference. Figure B5 shows comparisons of stirrup strains. Two stirrups in the test span yielded for both the model and specimen 10RA; however the yielded stirrups in the FE model were S1 and S2 stirrups, while the yielded stirrups in the 10RA beam were S2 and S3 stirrups. This difference may be due to actual discrete crack locations relative to strain gage locations and bond stresses adjacent to these crack locations compared to smeared cracking and perfect bond in the FE model.

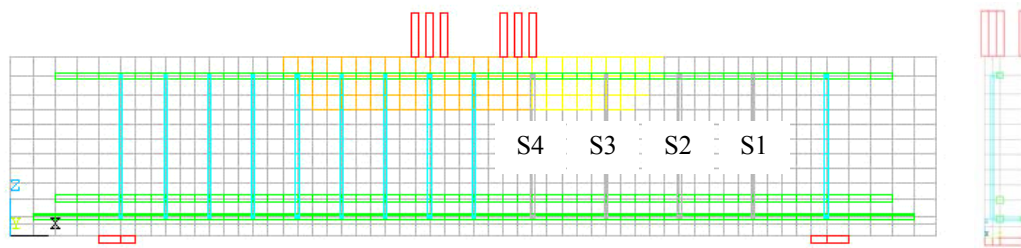
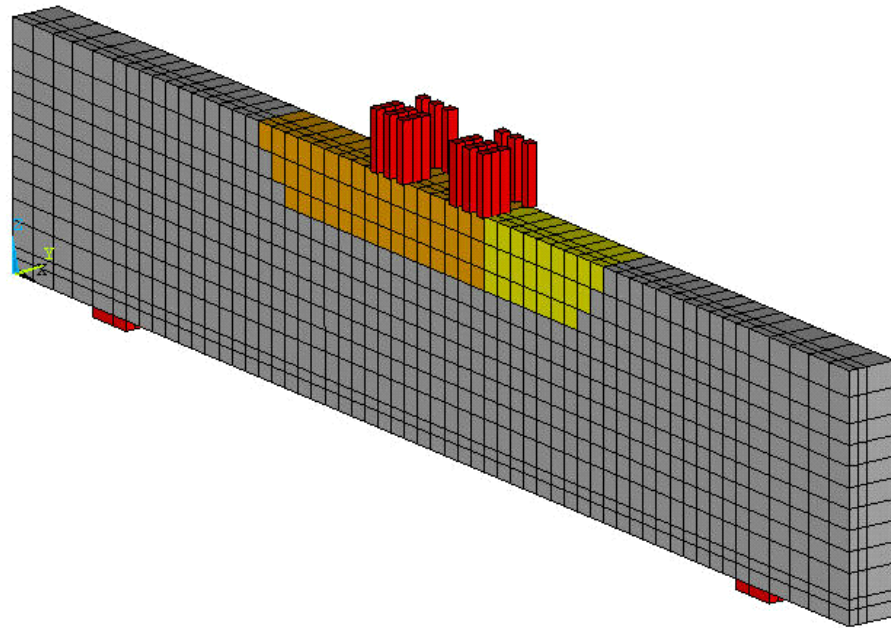
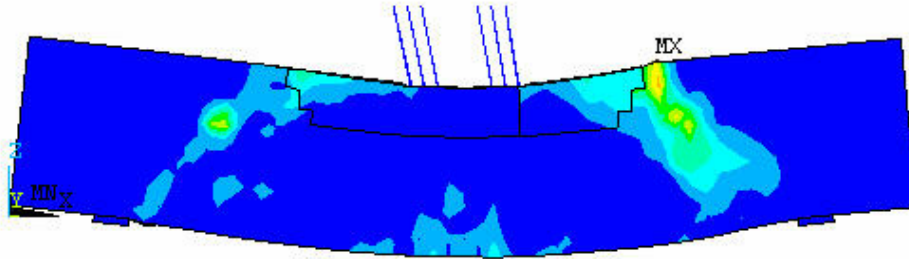
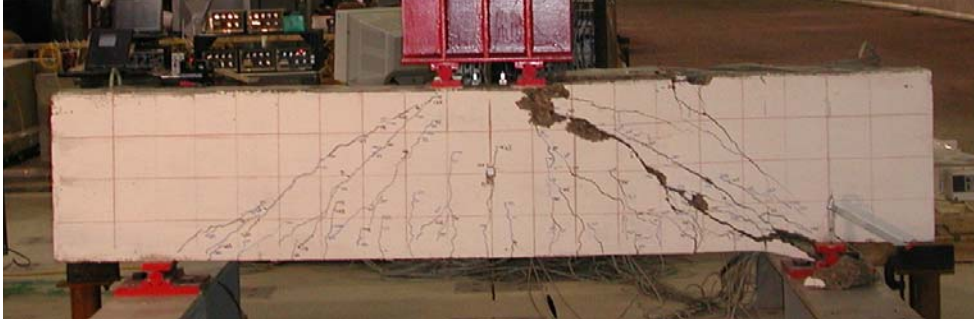
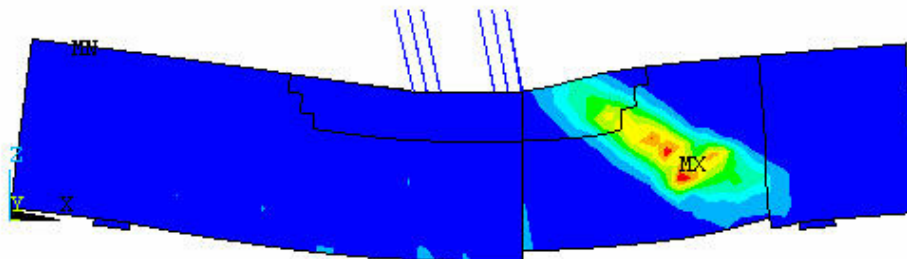


Figure B2: Undamaged finite element model



a)



b)

Figure B3: Crack patterns at failure: a) Specimen 10RA and undamaged FE model, b) Specimen 10RD and severely damaged FE model

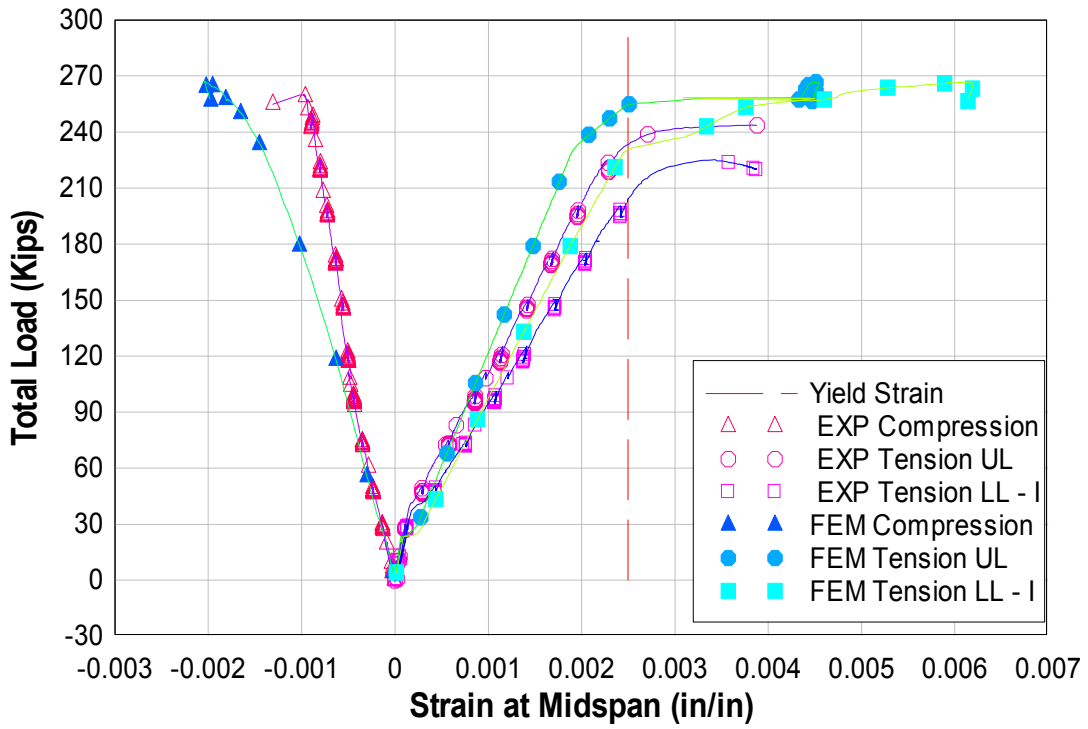


Figure B4: Flexural steel strains for experimental specimen 10RA and undamaged finite element model

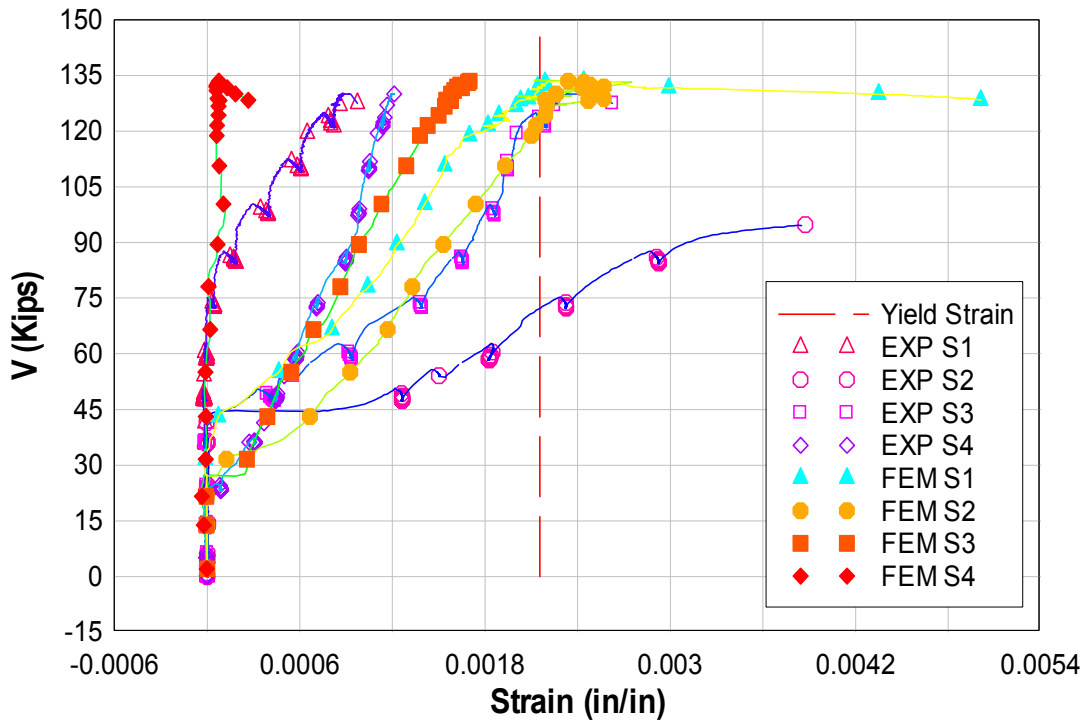


Figure B5: Stirrup strains for experimental specimen 10RA and undamaged finite element model

An FE model with severe corrosion damage was developed by removing 1-inch thick concrete elements at the outside layer (as shown in Figure B6) and eliminating the 4 stirrup elements in the test span. The maximum load and energy of the severely damaged model are 33% and 65% lower, respectively, than those of the undamaged model. The ultimate capacity and energy of the severely damaged model were 179.8 kips and 28.1 inch-kips, which are 2% and 6% lower than those of specimen 10RD. Load-deflection response of the severely damaged model is shown in Figure B1. Crack pattern comparisons between the FE model and specimen 10RD are shown in Figure B3b. One large crack is observed in specimen 10RD, while a wide band of large principal strains is seen in the FE model. Flexural and stirrup strains for specimen 10RD are not obtainable, since the strain gages were broken by the corrosion damage. Results from the undamaged model and severely damaged models matched experimental results of specimens 10RA and 10RD reasonably well, and indicated the upper and lower boundaries of the damage states.

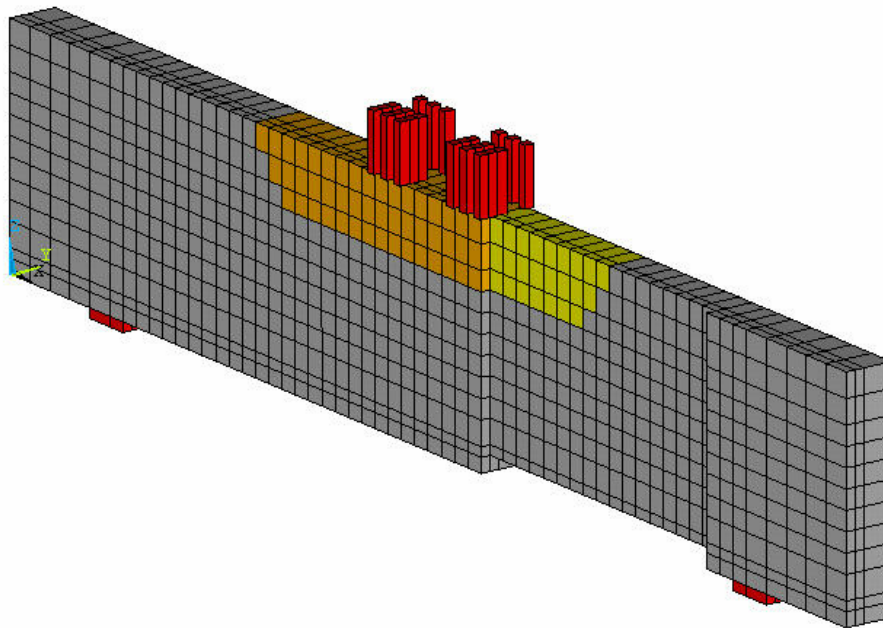


Figure B6: Corrosion-damaged finite element model with idealized concrete damage

To observe contributions from concrete cover spalling only, an outside layer of concrete elements was removed, while the stirrup elements were included in the model. The maximum load and energy of the model were reduced by 11% and 40%, respectively, as compared to the undamaged model.

FE models with only reduced average cross-sectional areas of stirrups were also developed. The cover spalling was ignored to observe the contribution of average stirrup cross-sectional loss to beam capacity. Areas of the stirrup truss elements in the test span were reduced by 50% and 100% uniformly over the entire length. The ultimate strength and energy of the models were 7% and 29% lower for the 50% section-loss model and 31% and 66% lower for the 100% section-loss model as compared to the undamaged FE model.

A combination of rebar section-loss and concrete cover spalling was also considered. Three average cross-sectional losses: 0%, 50%, and 100% were investigated. Load-deflection responses of the combined damage models are compared with those of the no-spall models with 0%, 50%, and 100% cross-sectional losses as shown in Figure B7. The ultimate load comparisons between the two model series are shown in Figure B8a. Ultimate load reductions of the no-spall models and cover spall models exhibited similar trends. A nonlinear reduction of ultimate loads occurs, when average section-loss for the stirrups in the models increase. For no-spall and spall models, 7% and 3% reductions of ultimate loads are found when average section-losses increase from 0% to 50%; and 26% and 22% reductions of ultimate loads are observed when average section-losses increase from 50% to 100%. Figure B8b displays a significance of the beam effective width to the energy of the models. When cover spall damage occurs, the energy of the model is 40% less than the energy of the undamaged model. When the average section-loss increases, the difference between the energies for the no-spall and spall models reduces, the 40% difference mentioned for 0% section-loss models, a 24% difference for 50% section-loss models, and a -1% difference for 100% section-loss models. For the 100% section-loss models, insignificant differences were observed for both the ultimate strength and energy, which were about 33% and 65% lower than those of the undamaged model. The analysis results are summarized in Table B2.

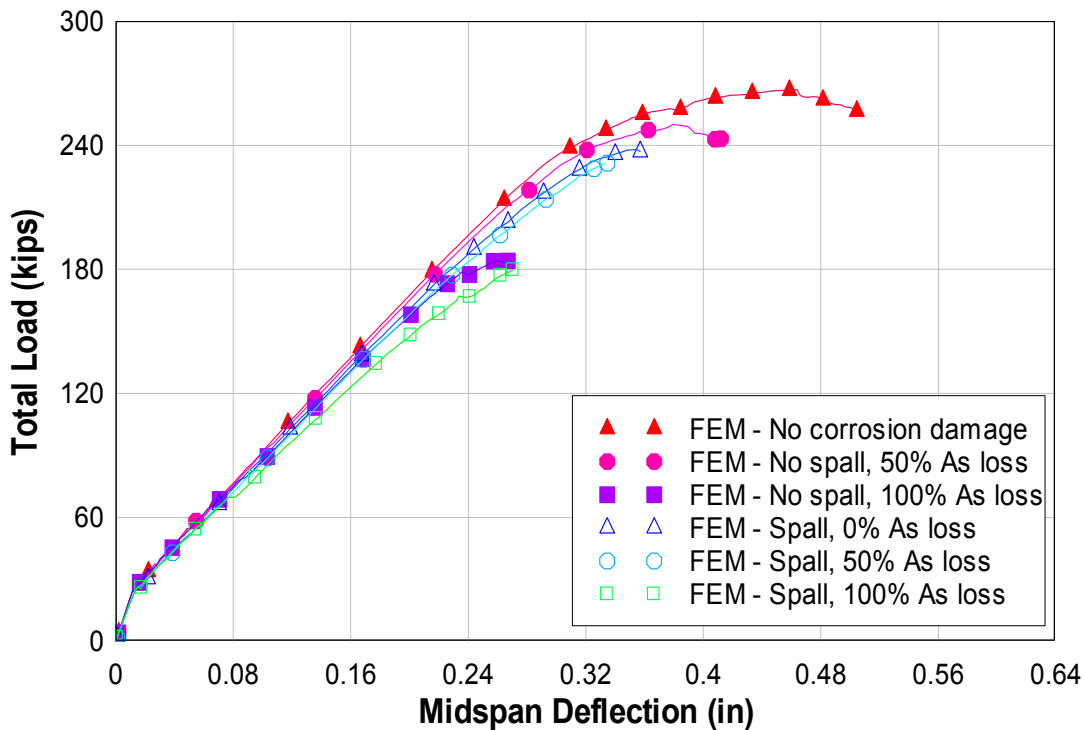
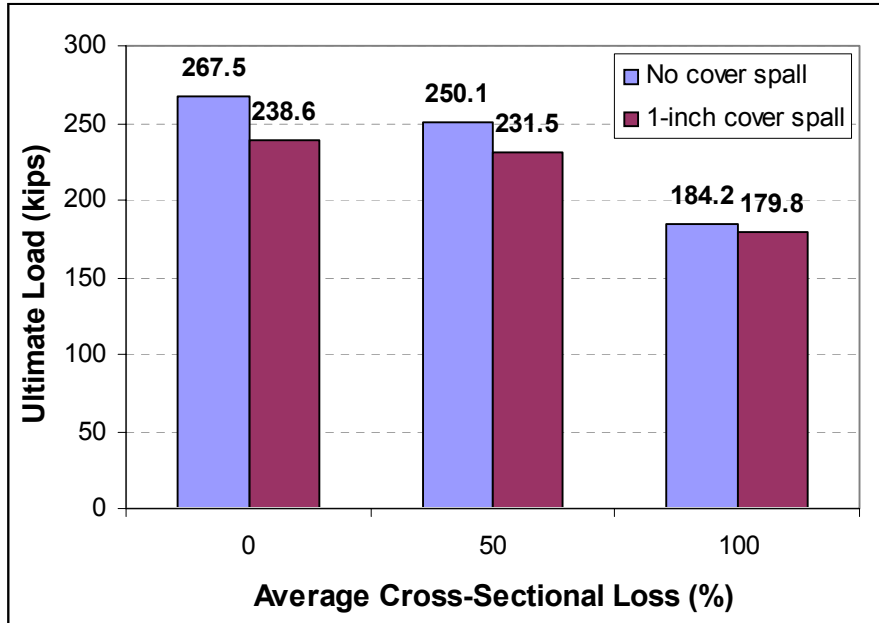
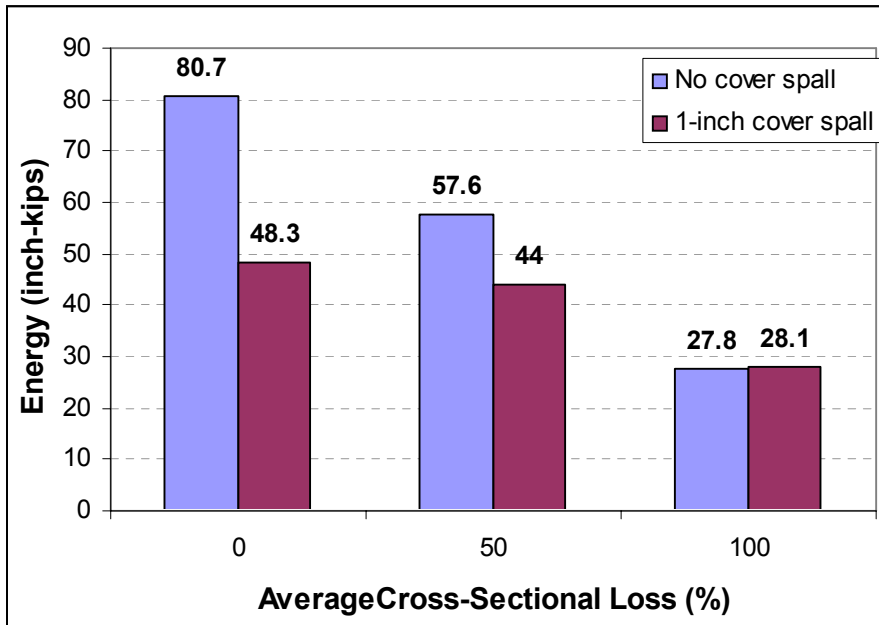


Figure B7: FE predicted load-deflection response for no-spall and spall models having 0%, 50%, and 100% average stirrup cross-sectional loss



a)



b)

Figure B8: FE summary result for no-spall and spall models: a) Ultimate load, b) Energy

Actual corroded stirrups may contain both uniform section-loss (called average for this study) and local maximum section-loss at a discrete location along the rebar. An FE model with concrete spalling was employed to determine the effects of locally reduced stirrup sections on structural performance. In this model, each stirrup was modeled using 9 finite truss elements. A

75% local maximum section-loss is applied to one of the 9 finite truss elements, with no section-loss for the other 8 truss elements. Different locations for local maximum section-loss within the test span were considered to characterize the influence of spacial damage sequencing on ultimate loads, energy, and crack patterns. Four models with different locations of local maximum loss, i.e. SP1, SP2, SP3, and SP4 models, were developed as shown in Figure B9. The maximum load, deflection at the maximum load, and energy results of the models are summarized in Table B3. Load-deflection responses of the models are shown in Figure B10. Ultimate loads of the SP1, SP2, and SP3 models were similar to each other and close to the ultimate load of the spall-only model, 2% higher for SP1 model and 1% less for SP2 and SP3 models. Energies of the SP1, SP2, and SP3 models were higher than the energy of the spall-only model, by 25%, 7%, and 2%, respectively. Vector plots of maximum principal strains were used for crack pattern comparisons. The local damage as indicated by rebar section-loss can produce a different crack pattern as shown in Figure B11 by comparing principal tensile strains of the SP1 model with the undamaged model. The ultimate load and energy of the SP4 model were 13% and 23% lower than those of the spall-only model. The SP4 model exhibited the lowest ultimate load and energy among the local section-loss models. The two locations of local section-loss were near or within the area of the beam with large principal strains (Figure B11). The sequencing of damage within this region contributed to diminished capacity and energy as the locally reduced sections in the compression strut zone fail to adequately constrain the transverse tensile strains.

**Table B3: Summary results for finite element models with spatially distributed stirrup local maximum cross-sectional loss**

<b>Model</b>	<b>Maximum Load (kips)</b>	<b>Deflection at Max. Load (inch)</b>	<b>Energy (inch-kips)</b>
SP1	244.3	0.401	60.5
SP2	236.0	0.365	51.5
SP3	235.8	0.356	49.5
SP4	206.5	0.305	37.1

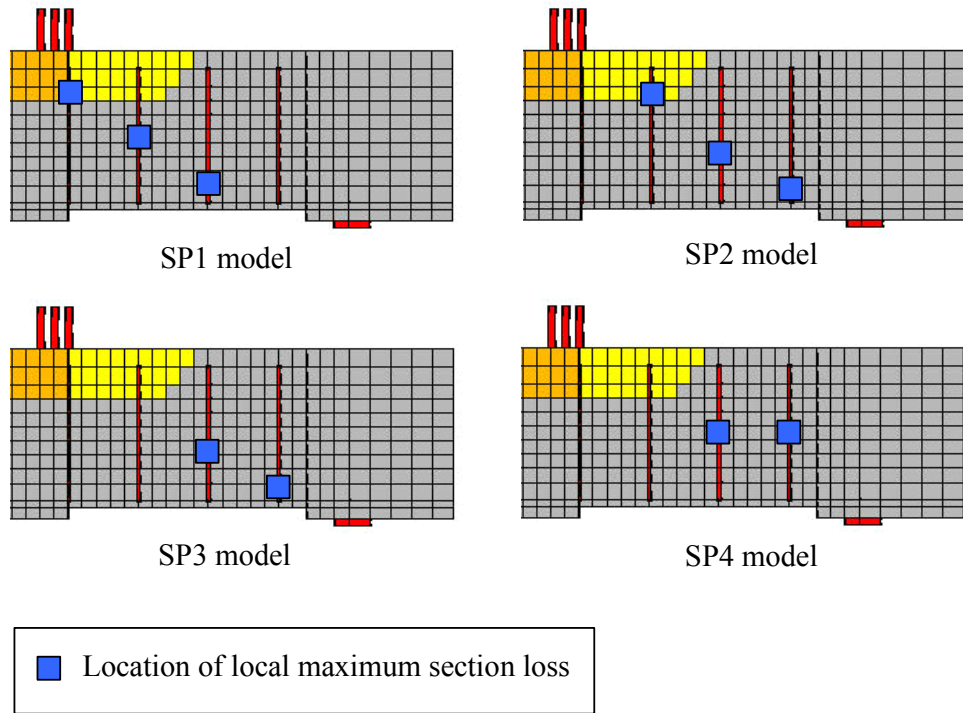


Figure B9: Finite element models with different spatial distribution of local maximum stirrup cross-sectional loss

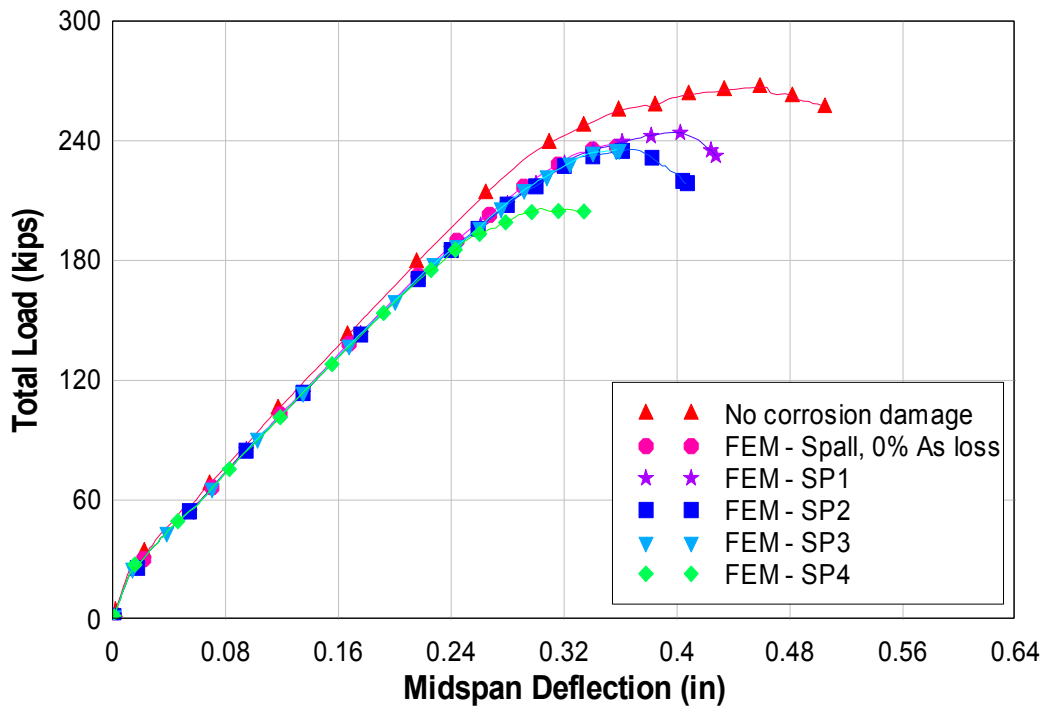
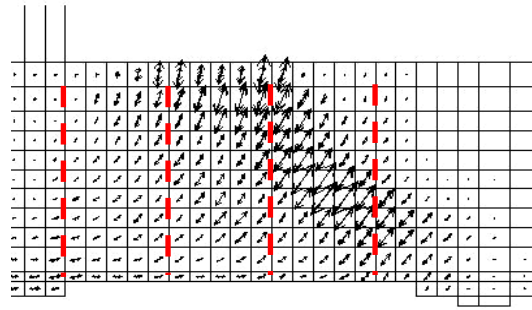
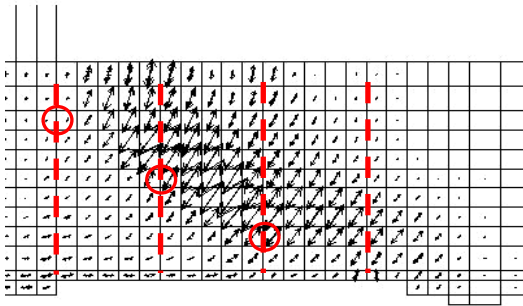


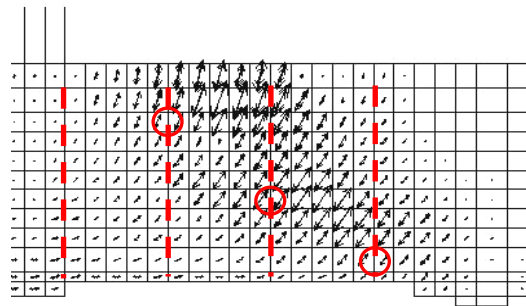
Figure B10: FE predicted load-deflection response for models with spatially distributed stirrup local maximum section loss



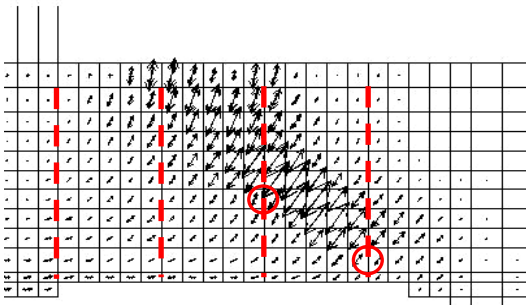
No stirrup section loss with  
concrete cover spalling



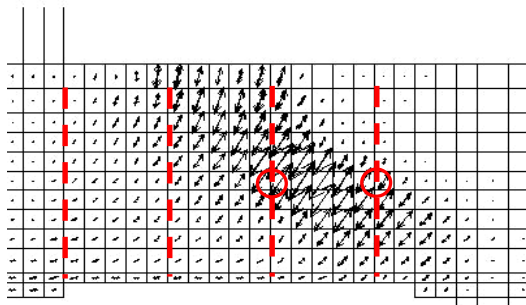
SP1 model



SP2 model



SP3 model



SP4 model

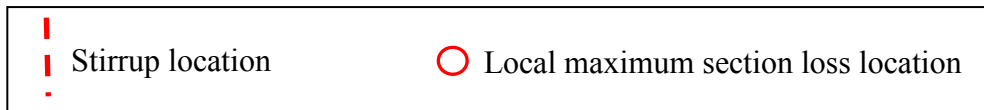


Figure B11: Vector plots of maximum principal strains for FE models with spatially distributed stirrup local maximum section loss (taken when maximum principal strain reaches approximately 0.03 anywhere in concrete cross-sections)

When average cross-sectional loss is added to the stirrups in the models with stirrup local maximum section-loss, capacity and energy reduction of the models can be augmented. Local maximum section-loss can occur randomly in corroded stirrups in bridge girders. The study

demonstrates that localized damage can result in reduced structural performance of corroded bridge girders when the locations of maximum section-loss occur adjacent to major shear cracks.

When concrete cover spalling takes place, bond at concrete-rebar interfaces is diminished. A combination of cover spalling and concrete-rebar interface debonding was included in a series of analyses. In the spall-only model each stirrup was modeled using 9 truss elements comprising 10 nodes. All nodes for the stirrup elements were constrained to solid concrete element nodes where they are coincident. To simulate concrete-rebar interface debonding due to corrosion, only the two nodes of the stirrup elements at both ends were connected to the concrete elements. Ultimate load and energy of the spalled concrete cover model with the debonded concrete-rebar interfaces were 23% and 54% lower than those of the undamaged model. Average stirrup section-loss of 50% was added to the spalled concrete cover model with debonded concrete-rebar interfaces. This model had an ultimate load reduction of 23% and an energy loss of 50% compared to the undamaged model. Debonded interfaces were also included for the local maximum loss using the SP2 model (average section-loss of 0% and local maximum section-loss of 75%). The SP2 model with concrete-rebar interface debonding had a capacity reduction of 28% and energy 61% lower than the undamaged model. An FE model considering concrete spalling, concrete-rebar interface debonding, average rebar section-loss of 50%, and local maximum rebar section-loss of 75% for the SP2 model was developed. The ultimate capacity and energy of the model were 32% and 63% less than those of the undamaged model. This damage combination can be typical for corrosion damage occurring in both experimental specimens and bridge girders. Results for models with debonded concrete-rebar interfaces are summarized in Table B2. Figure B12 shows load-deflection responses of the models with debonded concrete-rebar interfaces. As shown in the figure, the maximum load and energy of the models with the debonded concrete-rebar interfaces are relatively close to each other, and ranged from 23% to 32% for ultimate loads and 50% to 63% for energies less than the undamaged model.

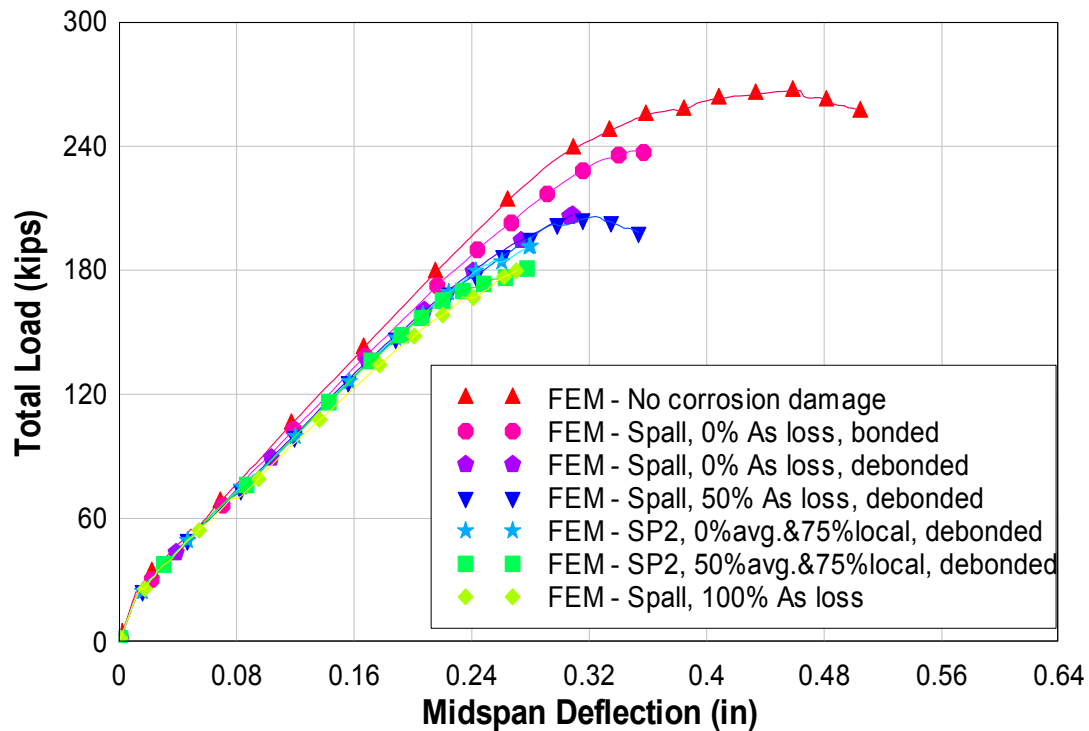


Figure B12: FE predicted load-deflection response for models with fully debonded concrete-rebar interface

Summary results of ultimate loads and energies for all finite element analyses and experimental data are shown in Figure B13. The sequence of results is sorted by the amount of energy dissipated for each case. The various corrosion damages modeled in the analysis were also ordered in their likely time of occurrence. The actual value of time (in years) will depend on many factors and is shown only qualitatively. Figure B14 illustrates possible sequencing of corrosion damage in time as a function of shear capacity obtained from the finite element analyses. The beam capacity is unchanged as chlorides reach threshold levels sufficient to cause corrosion at the stirrups. The time to initiation of corrosion is variable and depends on the concrete cover, environmental conditions, concrete permeability, etc. Once corrosion begins, concrete cover damage initiates due to expansion of corrosion reaction products. This damage to the concrete may occur soon after corrosion initiation. Following cover damage, the stirrups continue to lose cross-sectional area and this may take place with partial or complete debonding of the stirrup legs. Partial debonding may occur due to nonuniform corrosion along the stirrup length or due to no stirrup corrosion particularly in the upper portion of the girder stem. At the same time that average section-loss is taking place there may be locations with locally reduced cross-sectional areas. These three potential paths are shown in Figure B14 to illustrate these effects. The more likely path is the combined debonding, average section-loss and localized significant section-loss. Finally, the combined affect of these damage components will reduce the capacity to that of the most severely corroded damage observed through tests and by finite element prediction.

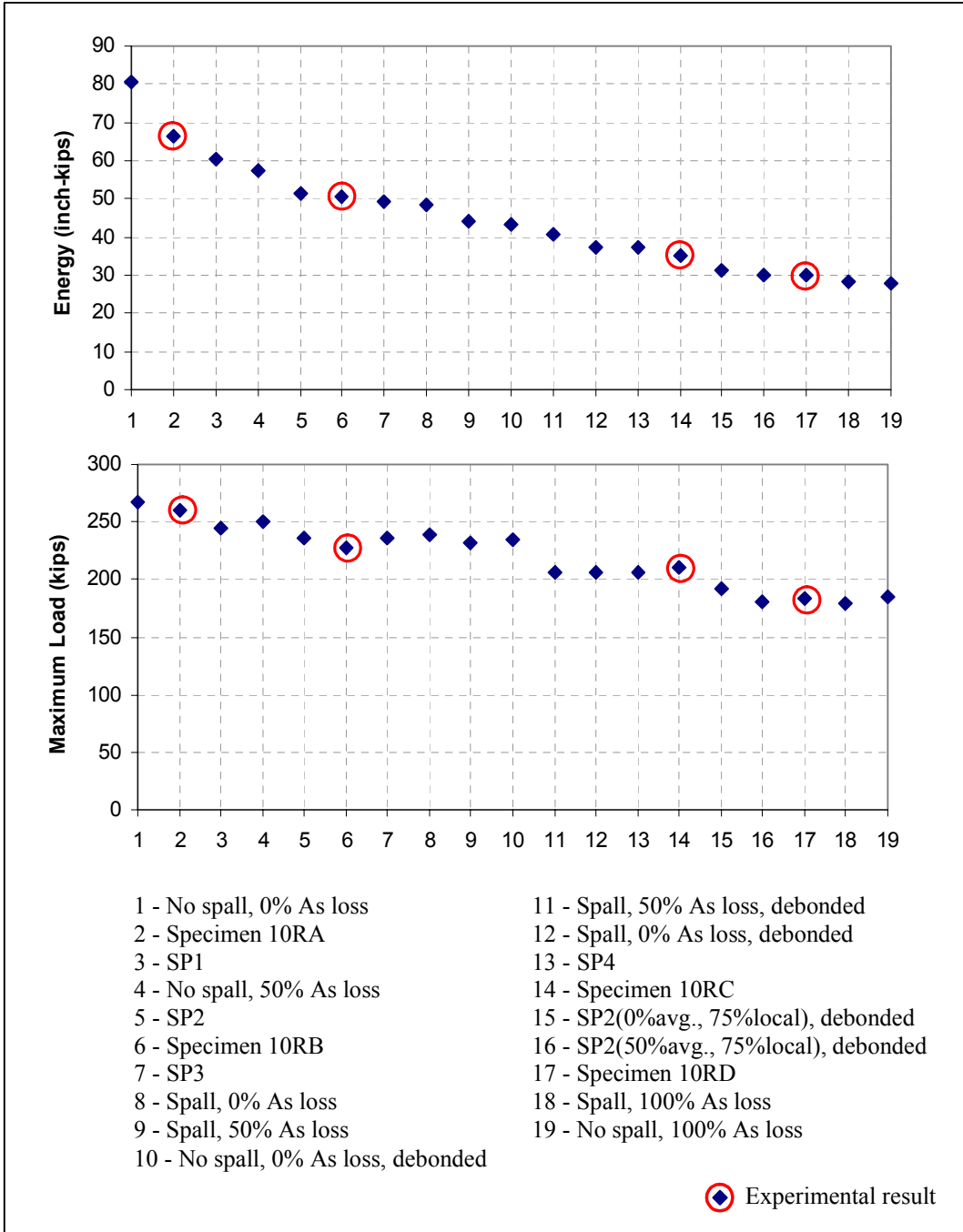


Figure B13: Summary results for maximum load and energy

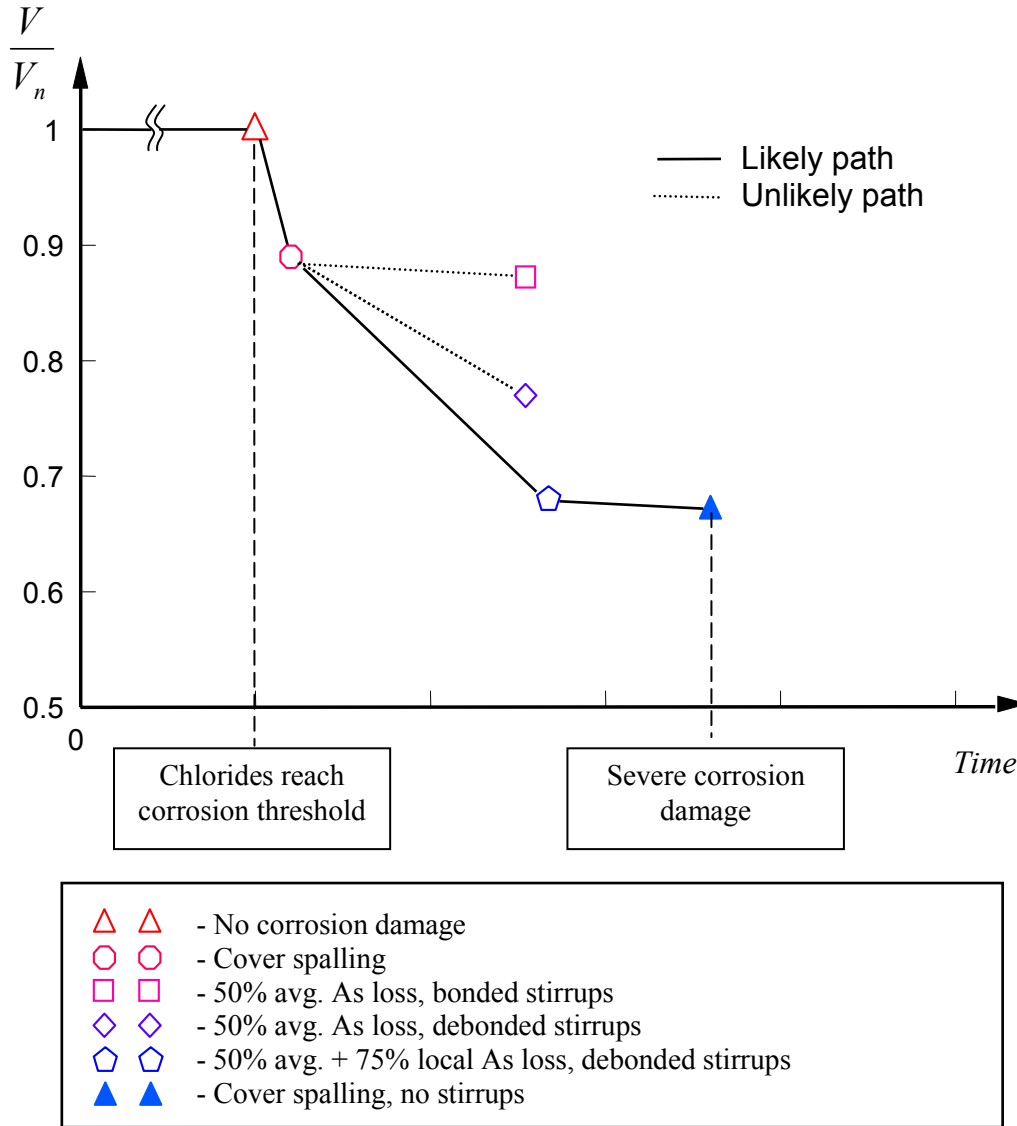


Figure B14: Corrosion damage sequence as a function of shear capacity

## Conclusions

Finite element modeling was used to isolate different contributions of corrosion damage to structural response of reinforced concrete beams failing in shear. Corrosion damage parameters included in the study were concrete section-loss due to spalling, average rebar cross-sectional loss, local maximum rebar cross-sectional loss and corresponding spacial distribution of maximum loss, and debonding of corrosion-damaged stirrups from the concrete. Models were compared with experimental results, and parametric studies were performed including both individual and combined corrosion induced damages. Based on FE analysis results, the following conclusions are made:

1. Results of the finite element models with no damage and severe damage (spalling and 100% average section-loss) matched the experimental results of specimens 10RA and 10RD reasonably well. Maximum load and energy of the undamaged model were 3% and 21% higher than those of specimen 10RA. Maximum load and energy of the severely damaged model were 2% and 6% lower than those of specimen 10RD.
2. Maximum load and energy of the severely damaged model were 33% and 65%, respectively, lower than those of the undamaged model.
3. Maximum load and energy of the spalled concrete cover model were 11% and 40%, respectively, lower than those of the undamaged model.
4. Maximum load and energy of the no-spall model with 100% average stirrup cross-sectional loss were 31% and 66%, respectively, lower than those of the undamaged model.
5. A nonlinear reduction of ultimate loads occurs, when average stirrup cross-sectional loss for the stirrups in the models increases. For no-spall and spall models, reductions of 7% and 3% are found when average section-losses increase from 0% to 50%; and reductions of 26% and 22% are observed when average section-losses increase from 50% to 100%.
6. SP1, SP2, and SP3 models with different locations for maximum section-loss had similar ultimate loads, which were 2% higher for the SP1 model and 1% lower for the SP2 and SP3 models than the ultimate load of the spall-only model. SP1, SP2, and SP3 model energies were 2% - 25% greater than the energy of the spall-only model.
7. The local damage as indicated by rebar section-loss can produce a different crack pattern for the SP1 model compared to the undamaged model.
8. The SP4 model had the lowest ultimate load and energy among the local section-loss models. The two local section-losses located in the compression strut zone may cause the lower ultimate load and energy, which are 13% and 23% lower than those of the spall-only model. Spacial distribution of corrosion damage can contribute to diminished structural performance.
9. Debonded concrete-rebar interfaces of the stirrups were included in average and local section-loss models yielding similar ultimate load and energy reductions, which were in a range of 23% - 32% lower for ultimate loads and a range of 50% - 63% lower for energy than those of the undamaged model.

**Appendix C**  
**Analysis Methods**

# Strut-and-Tie Method

## Introduction and Background

The Strut-and-Tie Method (STM) was recently adopted for use in ACI 318-02. This method is used for analysis of non-flexural members and for shear analysis when the clear span to height ratio ( $l_n/h$ ) is equal to or less than 4. The STM attempts to model the distribution of forces in the concrete section by idealizing the member as an equivalent truss consisting of compression force struts and tension ties. The struts and ties are connected by nodal regions which transfer forces between the internal elements as well as at external boundaries.

The strength of a strut depends on several factors and can be determined as:

$$F_{ns} = f_{cu} A_c \quad [C1]$$

$$f_{cu} = 0.85 \beta_s f'_c \quad [C2]$$

where  $f'_c$  is the compressive strength of the concrete,  $A_c$  is the area of the strut, and  $\beta_s$  a factor that accounts for cracking the strut may expect. Recommended  $\beta_s$  factors are shown in Table C1. The strength of tension ties is determined as:

$$F_{nt} = A_{st} f_y \quad [C3]$$

where  $A_{st}$  is the area of the reinforcing steel and  $f_y$  is the yield strength of the steel. Nodal strength is calculated as:

$$F_{nn} = f_{cu} A_n \quad [C4]$$

$$f_{cu} = 0.85 \beta_n f'_c \quad [C5]$$

where  $f'_c$  is the concrete compressive strength,  $A_n$  is the area of the node perpendicular to the line of action of the strut, tie, or external applied force, and  $\beta_n$  is a factor that accounts for the anchorage of ties at the nodal location. The factors recommended by ACI can be found in Table C2.

**Table C1: Factors for effective compressive strength of struts (ACI 318-02)**

Strut Type	$\beta_s$
Prismatic Strut	1.0
Bottle Strut with reinforcement	0.75
Bottle Strut without reinforcement	0.6
Struts in tension members	0.4
Other cases	0.6

**Table C2: Factors for effective compressive strength of nodal regions (ACI 318-02)**

Node Type	$\beta_n$
CCC Node	1.0
CCT Node	0.8
CTT Node	0.6

**STM Models for Test Specimens**

The STM was used to evaluate the shear strength of both corroded and uncorroded beams. Two different strut-and-tie models were developed as shown in Figs. C1a and C1b.

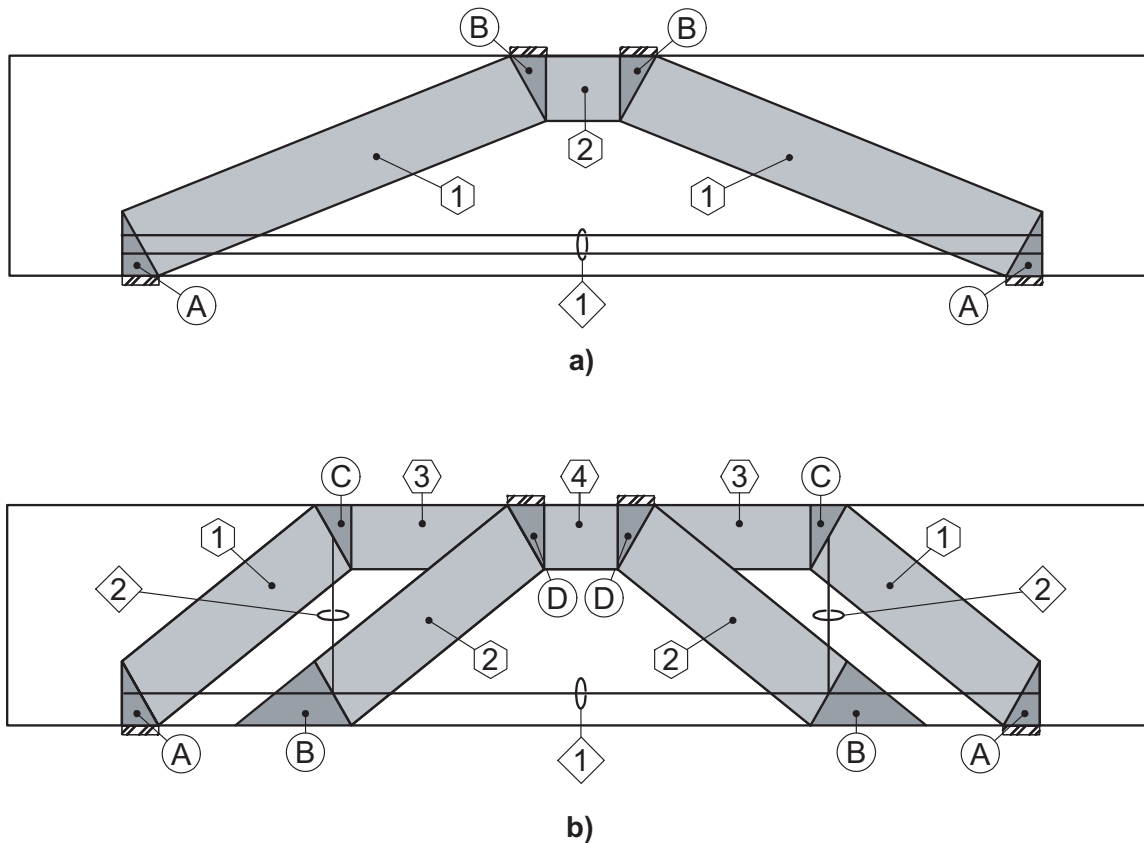


Figure C1: a) Strut-and-Tie model 'A', b) Strut-and-Tie model 'B'

The first model, STM-A, utilized three struts; two prismatic inclined struts (except for 10T Series where a bottle strut is required) and a prismatic strut between the loading points; one tension tie consisting of the flexural steel, and four nodes. The inclined compression strut, Strut 1, has an angle less than 25 degrees and does not meet the requirements of ACI 318 Appendix A (Marti,

1983). However, this model was evaluated as the simplest form of a strut-and-tie model for the beams.

Nodes at the reaction points (B in Figure C1a) were compression-compression-tension (CCT) nodes and at the loading points (A in Figure C1a) were compression-compression-compression (CCC) nodes. The size of Node A was determined by the length of the bearing plate ( $l_b$ ) and the width of the tie ( $w_t$ ), which was determined based on the distribution of flexural steel through the node. Application of the STM using the recommended factors in ACI 318-02 Appendix A predicts failure in the bottom CCT node. However, none of the beams tested failed due to a shear-tension failure, therefore the factor reducing the effective compressive strength in the CCT node was set to unity, which resulted in eventual failure of the inclined strut.

The width of the struts,  $w_s$ , was determined as:

$$w_s = w_t \cos \theta + l_b \sin \theta \quad [C6]$$

where  $\theta$  (degrees) is the angle of the strut,  $l_b$  is the length of the bearing plate (4 in. for all specimens), and  $w_t$  is the width of the tie region (7 in. for 8R, 10R, 10T, and 12R, where two layers of flexural steel were present). The strut angle for the beams was  $22^\circ$ , corresponding to a strut width of 8 in. For the 10IT series, the width of the tie region was 5 in. because the flexural steel was located in a single layer, resulting in a strut angle of  $24^\circ$  and corresponding to a strut width of 6.2 in. Node B was sized by setting the force couple from the flexural design equations to a maximum. This produced a 7 in. vertical height at Node B for specimens 8R, 10R, and 12R. The vertical height of Node B for specimen 10T was set equal to the deck thickness (4 in.) as the neutral axis was located in the deck. For specimen 10IT, the vertical height of Node B was 5 in. The length of the loading point at Node B is 4 in., thus making the width of the strut at the node 8 in. for 8R, 10R, 12R. The width of the strut was 5.6 in. for specimen 10T and 6.2 in. for specimen 10IT.

Strut sizes were determined based on nodal sizes determined above. The width of Strut 1 and Strut 2 for specimens 8R, 10R, 12R, was 8 and 7 in., respectively. For specimen 10T, the width of Strut 2 was 4 in. and a bottle strut was used for Strut 1, because the width of Node A was 8 in. and the width of Node B was 4 in. As a consequence, the stress in the bottle strut was checked at each end. For specimen 10IT, the width of Struts 1 and 2 were 6.2 and 5 in., respectively. The area of Tie 1 was  $3.95 \text{ in}^2$  for all specimens.

The second model, STM-B, consists of four inclined struts, three horizontal struts, three tension ties, and eight nodes. The first tension tie (Tie 1) consists of the flexural steel and the second two tension ties (Tie 2) represent the shear reinforcement. The amount of shear reinforcement included in Tie 2 is the area of stirrups that cross both inclined struts. The eight nodes consist of four CCT nodes (A and C in Figure C1b), two CTT nodes (B in Figure C1b), and two CCC nodes (D in Figure C1b). Applying the ACI recommended  $\beta_n$  factors to the nodes resulted in failure at the CTT node (Node B) that was not observed in the tests. Setting the  $\beta_n$  factor for this node to unity caused failure in the two CCT nodes (Node A) at the bearing plates (which was also not observed in the tests), therefore,  $\beta_n$  factors for these nodes were also set to unity. Eventually, failure occurred in the two inclined struts or in Tie 2.

The size of Node A was determined in the same manner as described for STM-A. The size of Node A for 8R, 10R, 10T, and 12R was 5.7 in. This was calculated using Eq. C6 and the length of bearing (4 in.), the width of the tie (7 in.), and the angle of the strut which was 39°. For beam series 10IT, the width of the tie was 5 in. and the angle of the strut was 42° making the width of the strut 6.4 in.

Node B was sized so that the width of the node bearing against Strut 2 was the same size, making it 5.7 in. for 8R, 10R, 10T, and 12R. This node width was 6.4 in. for specimen 10IT. Nodes C and D were the same size as determined for STM-A. The width of Strut 1 was 5.7 in. for 8R, 10R, 10T, and 12R; and 6.4 in. for specimen 10IT. For the face bearing against Strut 3, the width was 7, 4, and 5 in., respectively. For Node D the length of the bearing plate was 4 in. for all beams. The width of the node bearing against Strut 2 was 5.7 in. for 8R, 10R, and 10T, and 12R; and 6.4 in. for specimen 10IT. The width of Node D bearing against Strut 4 was 7 in. for 8R, 10R, and 12R; 4 in. for specimen 10T; and 5 in. for specimen 10IT.

The widths of the struts were determined from the nodal geometry. For beam series 8R, 10R, and 12R the struts were all assumed to be prismatic with widths of 5.7 in. for Struts 1 and 2 and 7 in. for Struts 3 and 4. For the 10T series, Struts 1 and 2 had a width of 5.7 in., while Struts 3 and 4 were 4 in. wide. The width of for Struts 1 and 2 was 6.4 in. and the width of Struts 3 and 4 was 5 in. for the 10IT series.

The area of Tie 1 for STM-B was the same for all beams, as described for STM-A. Tie 2 represents the shear stirrups and the area varied depending on stirrup spacing. Tie 2 was 2.4 in<sup>2</sup> (6 stirrups), 2.0 in<sup>2</sup> (5 stirrups), and 1.6 in<sup>2</sup> (4 stirrups) for beams with 8, 10, and 12 in. stirrup spacing, respectively.

Predicted shear strength for the undamaged beams is shown in Table C3 for STM-A models and in Table C4 for STM-B models. As seen in these tables, STM-B reasonably estimated the shear strength for all the undamaged beam configurations. STM-A predicted shear capacity reasonably well for the rectangular beams, but significantly under-estimated the strength of the T and IT series. The STM-A model had a mean  $V_{\text{Experiment}}/V_{\text{Predicted}}$  value of 1.26 with a coefficient of variation of 0.23 for undamaged models. The STM-B model had an average  $V_{\text{Experiment}}/V_{\text{Predicted}}$  equal to 1.05 with a coefficient of variation of 0.04 for undamaged models.

**Table C3: Shear strength prediction for undamaged STM-A models**

Beam	$b_w$ [in]	$b_e$ [in]	Nodes				Strut				Tie $F_{nt1}$ [kips]	$V_{STM}$ [kips]	$V_{EXP}/V_{STM}$
			$\beta_n$ -	$F_{n1}$ [kips]	$\beta_n$ -	$F_{n2}$ [kips]	$\beta_s$ -	$F_{ns1}$ [kips]	$\beta_s$ -	$F_{ns2}$ [kips]			
8RA	10.0	10.0	1.0	110.8	1.0	110.8	1.0	110.8	1.0	640.6	703.9	110.8	1.20
10RA	10.0	10.0	1.0	126.1	1.0	126.1	1.0	126.1	1.0	728.9	703.9	126.1	1.03
10TA	10.0	10.0	1.0	122.3	1.0	112.3	0.8	84.3	1.0	403.9	703.9	84.3	1.68
10ITA	10.0	10.0	1.0	95.8	1.0	95.8	1.0	95.8	1.0	412.1	626.9	95.8	1.41
12RA	10.0	10.0	1.0	112.1	1.0	112.1	1.0	112.1	1.0	648.0	703.9	112.1	0.98

**Table C4: Shear strength prediction for undamaged STM-B models**

Beam	$b_w$ [in]	$b_e$ [in]	Nodes								Strut								Tie		$V_{STM}$ [kips]	$V_{EXP}/V_{STM}$
			$\beta_n$ -	$F_{n1}$ [kips]	$\beta_n$ -	$F_{n2}$ [kips]	$\beta_n$ -	$F_{n3}$ [kips]	$\beta_n$ -	$F_{n4}$ [kips]	$\beta_s$ -	$F_{ns1}$ [kips]	$\beta_s$ -	$F_{ns2}$ [kips]	$\beta_s$ -	$F_{ns3}$ [kips]	$\beta_s$ -	$F_{ns4}$ [kips]	$F_{nt1}$ [kips]	$F_{nt2}$ [kips]		
8RA	10.0	10.0	1.0	133.1	1.0	132.6	1.0	132.6	1.0	132.6	1.0	132.6	1.0	132.6	1.0	319.6	1.0	319.6	351.2	153.6	132.6	1.01
10RA	10.0	10.0	1.0	151.5	1.0	150.9	1.0	150.9	1.0	150.9	1.0	150.9	1.0	150.9	1.0	363.7	1.0	363.7	351.2	128.0	128.0	1.02
10TA	10.0	10.0	1.0	146.9	1.0	146.4	1.0	188.7	1.0	188.7	1.0	146.4	1.0	146.4	1.0	262.0	1.0	262.0	351.2	128.0	128.0	1.11
10ITA	10.0	10.0	1.0	149.6	1.0	160.2	1.0	160.2	1.0	149.6	1.0	160.2	1.0	160.2	1.0	207.6	1.0	207.6	315.7	128.0	128.0	1.05
12RA	10.0	10.0	1.0	134.7	1.0	134.2	1.0	134.2	1.0	134.2	1.0	134.2	1.0	134.2	1.0	323.3	1.0	323.3	351.2	102.4	102.4	1.07

## Modeling Corrosion Damage with STM

Corrosion damage effects were incorporated in the STM by modifying two model attributes. Tension tie areas were reduced to reflect stirrup cross-sectional loss. Strut widths were also reduced to reflect concrete cover damage due to spalling. Effective concrete widths were calculated by Eq. 16b. Corrosion damage to the stirrups was considered in two ways, (1) the average section-loss along the length of the stirrups crossing the inclined struts (by Eqs. 11 to 13), and (2) the average of the local minimum stirrup areas crossing the inclined struts (Eqs. 11 and 14 to 15). Model properties for STM-B are shown in Tables C5 and C6. The STM model A did not have vertical tension ties representing the stirrup contribution and therefore corrosion damage to the stirrups could not be incorporated into this model. However, concrete cover damage could be modeled by using a reduced beam width. Results for STM model A with corrosion damage to the concrete cover are shown in Figure C2.

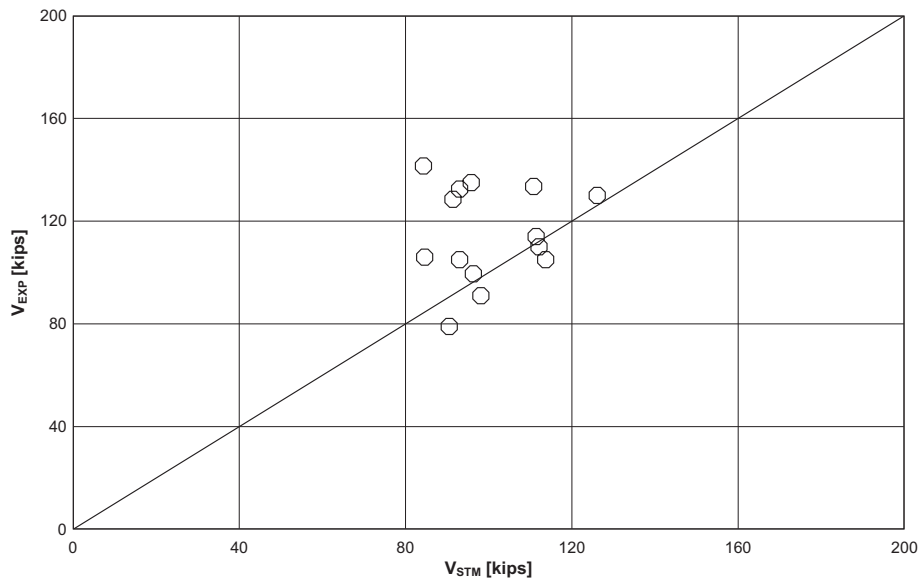


Figure C2: Experimental and analytical prediction of shear capacity using Strut-and-Tie Method Model A (corrosion damage to effective beam width only, as no vertical tension ties are used in the model)

Shear capacity of the corrosion damaged beams was fairly well predicted for the STM model B using the theoretical effective beam web width and the average cross section-loss as shown in Table C5 and Figure C3a. The STM-B model with average stirrup area had a mean value of  $V_{Experiment}/V_{Predicted} = 1.13$  with a coefficient of variation of 0.16. By comparison, the same model using reduced vertical tension tie area according to the local minimum stirrup area tended to under estimate capacity more significantly and exhibited larger scatter as shown in Table C6 and shown in Figure C3b. The STM-B model with local minimum stirrup area had a  $V_{Experiment}/V_{Predicted}$  mean value of 1.79 and the coefficient of variation was 0.66.

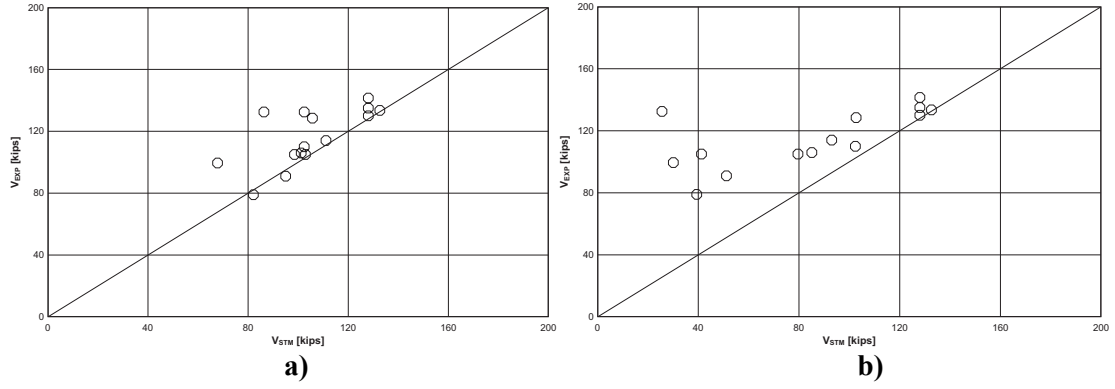


Figure C3: Experimental and analytical prediction of shear capacity from Strut-and-Tie Method model B

**Table C5: Shear design prediction for STM-B using with damage attributed to concrete with *average* section-loss**

Beam	f <sub>c</sub> [psi]	b <sub>e</sub> [in]	Nodes				Strut				Tie		V <sub>STM</sub> [kips]	V <sub>STM</sub> /V <sub>EXP</sub>		
			β <sub>n</sub> -	F <sub>n1</sub> [kips]	F <sub>n2</sub> [kips]	F <sub>n3</sub> [kips]	F <sub>n4</sub> [kips]	β <sub>s</sub> -	F <sub>ns1</sub> [kips]	F <sub>ns2</sub> [kips]	F <sub>ns3</sub> [kips]	F <sub>ns4</sub> [kips]			F <sub>nt1</sub> [kips]	F <sub>nt2</sub> [kips]
8RA	4350	10.0	1.0	133.1	132.6	132.6	132.6	1.0	132.6	132.6	319.6	319.6	351.2	153.6	132.6	1.01
8RD	4150	8.0	1.0	101.6	101.2	101.2	101.2	1.0	101.2	101.2	244.0	244.0	351.2	109.2	101.2	1.05
10RA	4950	10.0	1.0	151.5	150.9	150.9	150.9	1.0	150.9	150.9	363.7	363.7	351.2	128.0	128.0	1.02
10RB	5000	8.75	1.0	133.9	133.4	133.4	133.4	1.0	133.4	133.4	321.5	321.5	351.2	111.1	111.1	1.03
10RC	5100	8.75	1.0	136.6	136.1	136.1	136.1	1.0	136.1	136.1	327.9	327.9	351.2	98.5	98.5	1.07
10RD	4400	8.75	1.0	117.8	117.4	117.4	117.4	1.0	117.4	117.4	282.9	282.9	351.2	95.0	95.0	0.96
10TA	4800	10.0	1.0	146.9	146.4	166.9	166.9	1.0	146.4	146.4	231.8	231.8	351.2	128.0	128.0	1.11
10TC	5300	8.75	1.0	141.9	141.4	184.3	184.3	1.0	141.4	141.4	255.9	255.9	351.2	102.9	102.9	1.02
10TD	5300	8.75	1.0	141.9	141.4	184.3	184.3	1.0	141.4	141.4	255.9	255.9	351.2	86.3	86.3	1.54
10ITA	4400	10.0	1.0	149.6	160.2	160.2	149.6	1.0	160.2	160.2	207.6	207.6	315.7	128.0	128.0	1.05
10ITC	4800	8.75	1.0	142.8	152.9	152.9	142.8	1.0	152.9	152.9	198.1	198.1	315.7	105.7	105.7	1.22
10ITD	4750	8.75	1.0	141.3	142.3	142.3	141.3	1.0	151.3	151.3	196.1	196.1	315.7	82.1	82.1	0.96
12RA	4400	10.0	1.0	134.7	134.2	134.2	134.2	1.0	134.2	134.2	323.3	323.3	351.2	102.4	102.4	1.07
12RD	4200	9.0	1.0	115.7	115.3	115.3	115.3	1.0	115.3	115.3	277.8	277.8	351.2	67.8	67.8	1.47
12RA(D)	4750	10.0	1.0	161.5	172.9	172.9	161.5	1.0	172.9	172.9	224.1	224.1	189.4	102.4	102.4	1.29

**Table C6: Shear design prediction for STM-B using with damage attributed to concrete with *local minimum* stirrup area**

Beam	f' <sub>c</sub> [psi]	b <sub>e</sub> [in]	Nodes				Strut				Tie		V <sub>STM</sub> [kips]	V <sub>STM</sub> /V <sub>EXP</sub>		
			β <sub>n</sub> -	F <sub>n1</sub> [kips]	F <sub>n2</sub> [kips]	F <sub>n3</sub> [kips]	F <sub>n4</sub> [kips]	β <sub>s</sub> -	F <sub>ns1</sub> [kips]	F <sub>ns2</sub> [kips]	F <sub>ns3</sub> [kips]	F <sub>ns4</sub> [kips]			F <sub>nt1</sub> [kips]	F <sub>nt2</sub> [kips]
8RA	4350	10.0	1.0	133.1	132.6	132.6	132.6	1.0	132.6	132.6	319.6	319.6	351.2	153.6	132.6	1.01
8RD	4150	8.0	1.0	101.6	101.2	101.2	101.2	1.0	101.2	101.2	244.0	244.0	351.2	85.1	85.1	1.25
10RA	4950	10.0	1.0	151.5	150.9	150.9	150.9	1.0	150.9	150.9	363.7	363.7	351.2	128.0	128.0	1.02
10RB	5000	8.75	1.0	133.9	133.4	133.4	133.4	1.0	133.4	133.4	321.5	321.5	351.2	93.0	93.0	1.23
10RC	5100	8.75	1.0	136.6	136.1	136.1	136.1	1.0	136.1	136.1	327.9	327.9	351.2	79.6	79.6	1.32
10RD	4400	8.75	1.0	117.8	117.4	117.4	117.4	1.0	117.4	117.4	282.9	282.9	351.2	51.2	51.2	1.78
10TA	4800	10.0	1.0	146.9	146.4	166.9	166.9	1.0	146.4	146.4	231.8	231.8	351.2	128.0	128.0	1.11
10TC	5300	8.75	1.0	141.9	141.4	184.3	184.3	1.0	141.4	141.4	255.9	255.9	351.2	41.3	41.3	2.54
10TD	5300	8.75	1.0	141.9	141.4	184.3	184.3	1.0	141.4	141.4	255.9	255.9	351.2	25.6	25.6	5.18
10ITA	4400	10.0	1.0	149.6	160.2	160.2	149.6	1.0	160.2	160.2	207.6	207.6	315.7	128.0	128.0	1.05
10ITC	4800	8.75	1.0	142.8	152.9	152.9	142.8	1.0	152.9	152.9	198.1	198.1	315.7	102.7	102.7	1.25
10ITD	4750	8.75	1.0	141.3	142.3	142.3	141.3	1.0	151.3	151.3	196.1	196.1	315.7	39.4	39.4	2.01
12RA	4400	10.0	1.0	134.7	134.2	134.2	134.2	1.0	134.2	134.2	323.3	323.3	351.2	102.4	102.4	1.07
12RD	4200	9.0	1.0	115.7	115.3	115.3	115.3	1.0	115.3	115.3	277.8	277.8	351.2	30.1	30.1	3.31

## Modified Compression Field Theory (MCFT)

Modified Compression Field Theory (MCFT) (Vecchio and Collins, 1986) is the shear design methodology prescribed by the AASHTO LRFD Bridge Design Specification. MCFT takes into account residual concrete stresses in cracked concrete that permit the concrete section to resist higher shear forces. The model simplifies the complex shear behavior of a beam into a series of parallel diagonal cracks at an angle  $\theta$  from horizontal, and assumes average stresses exist on the cross-section. MCFT may not predict shear capacity well for elements with an  $a/d$  ratio less than 2.5 (ASCE-ACI Committee 445, 1999). The  $a/d$  ratio of the tested beams was 2.0. Therefore, while MCFT may not adequately predict the shear capacity of the specimens, it is used to demonstrate how corrosion damage can be incorporated into MCFT (results shown subsequently indicate that MCFT did predict shear capacity of the specimens reasonably well).

The shear capacity for a nonprestressed concrete beam is computed as in Eq. 7, but stirrup and concrete strength contributions depend on the crack angle and average strain on the section as:

$$V_s = \frac{A_v f_y d_v \cot(\theta)}{s} \quad \text{for straight leg stirrups} \quad [C7]$$

$$V_c = \beta \sqrt{f'_c} b_v d_v \quad [C8]$$

where  $A_v$  is the area of stirrups,  $f_y$  is the yield stress of the stirrups,  $s$  is the stirrup spacing,  $b_v$  is the effective width of the beam,  $d_v$  is the distance between compression and tension resultants from moment equilibrium,  $f'_c$  is the concrete compressive strength, and  $\beta$  is a factor related to  $\theta$  the crack angle, and  $\varepsilon_x$  the average longitudinal strain in the section. When the cross-section has at least minimum stirrups, the average longitudinal strain can be determined as:

$$\varepsilon_x = \frac{\frac{M_u}{d_v} + 0.5(V_u \cot(\theta))}{2E_s A_s} \leq 0.002 \quad [C9]$$

where  $M_u$  is the factored applied moment,  $V_u$  is the factored applied shear,  $A_s$  is the area of flexural steel that is adequately developed at the section, and  $E_s$  is the modulus of elasticity for the flexural steel. If the section has less than minimum area of stirrups, Eq. C9 is multiplied by 2. Minimum stirrup area is defined as:

$$A_v = \left(\frac{1}{1000}\right) \sqrt{f'_c} \frac{b_v s}{f_y} \quad (\text{units for } f_y \text{ and } f'_c \text{ are psi}) \quad [C10]$$

Values of  $\beta$  and  $\theta$  are chosen from tables within the AASHTO code and the capacity of the section is computed. Alternatively, Response 2000<sup>TM</sup> (described below) may be used to compute the shear-moment interaction curve.

Corrosion damage is incorporated by reducing the beam effective width and considering two different types of damage to the stirrups: average area and minimum area. Predictions of shear capacity using the average stirrup section-loss are shown in Table C7 and Figure C4a. MCFT

with average stirrup area provided  $V_{EXPERIMENT}/V_{MCFT} = 1.40$  and a coefficient of variation of 0.16. MCFT using local minimum area tended to under-estimate shear capacity and had larger scatter as shown in Table C8 and Figure C4b. The average value of the  $V_{EXPERIMENT}/V_{MCFT} = 1.79$  with a coefficient of variation of 0.55.

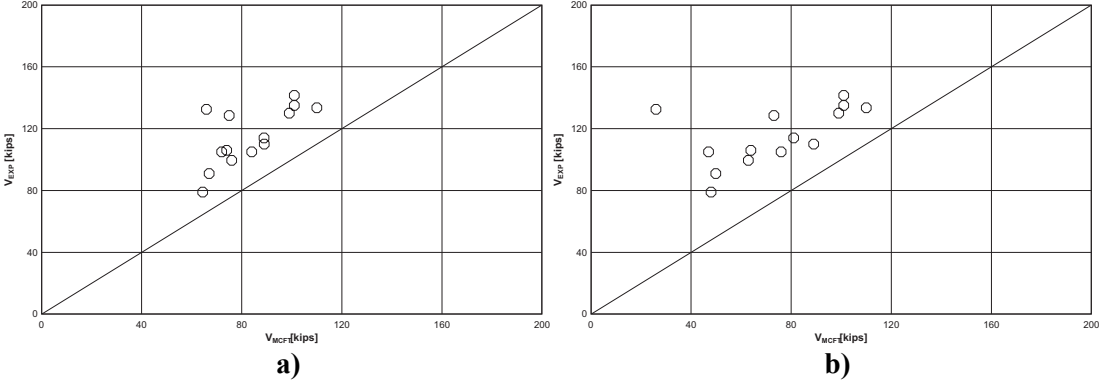


Figure C4: Experimental and analytical prediction of shear capacity from MCFT

**Table C7: MCFT Results using the proposed corrosion damaged model with *average* section-loss**

Beam	$f'_c$	$b_e$	$d$	$b_w d$	$\rho$	$A_v$	$f_{yv}$	$s$	$V_s$	$V_c$	$V$ [kips]	
	[psi]	[in]	[in]	[in <sup>2</sup> ]	-	[in <sup>2</sup> ]	[ksi]	[in]	[kips] MCFT	[kips] MCFT	$V/V_{EXP}$	MCFT
8RA	4350	10	20.5	205	0.019	0.4	64	8	83.4	26.6	110.0	1.21
8RD	4150	8.5	20.5	143.5	0.019	0.2844	64	8	54.6	19.4	74.0	1.43
10RA	4950	10	20.5	205	0.019	0.4	64	10	69.3	29.7	99.0	1.31
10RB	5000	8.75	20.5	157.85	0.019	0.3472	64	10	63.0	25.9	88.9	1.28
10RC	5100	8.75	20.5	143.5	0.019	0.3077	64	10	57.1	26.9	84.0	1.25
10RD	4400	8.75	20.5	143.5	0.019	0.2969	64	10	46.2	20.8	67.0	1.36
10TA	4800	10.0	20.5	205	0.018	0.400	64	10	69.6	31.4	101.0	1.40
10TC	5300	8.75	20.5	143.5	0.019	0.319	64	10	49.6	22.4	72.0	1.46
10TD	5300	8.75	20.5	143.5	0.019	0.270	64	10	42.5	23.4	65.9	2.01
10ITA	4400	10.0	21.5	215	0.019	0.400	64	10	72.0	29.0	101.0	1.34
10ITC	4800	8.75	21.5	150.5	0.018	0.330	64	10	52.7	22.3	75.0	1.71
10ITD	4750	8.75	21.5	150.5	0.018	0.257	64	10	42.1	22.3	64.4	1.23
12RA	4400	10.0	20.5	205	0.019	0.400	64	12	61.0	28.0	89.0	1.24
12RD	4200	9.0	20.5	143.5	0.019	0.265	64	12	47.1	28.9	76.0	1.31

**Table C8: MCFT Results using the proposed corrosion damaged model with *minimum* cross-section**

Beam	f <sub>c</sub>	b <sub>e</sub>	d	b <sub>w</sub> d	ρ	A <sub>v</sub>	f <sub>yv</sub>	s	V <sub>s</sub>	V <sub>c</sub>	V <sub>EXP</sub>	V [kips] V/V <sub>EXP</sub> MCFT	
	[psi]	[in]	[in]	[in <sup>2</sup> ]	-	[in <sup>2</sup> ]	[ksi]	[in]	[kips] MCFT	[kips] MCFT	[kips]		
8RA	4350	10	20.5	205	0.019	0.4	64	8	83.4	26.6	133.5	110.0	1.21
8RD	4150	8.5	20.5	143.5	0.019	0.2217	64	8	43.9	20.0	106.0	63.9	1.66
10RA	4950	10	20.5	205	0.019	0.4	64	10	69.3	29.7	130.0	99.0	1.31
10RB	5000	8.75	20.5	157.85	0.019	0.2906	64	10	54.2	26.8	114.0	81.0	1.41
10RC	5100	8.75	20.5	143.5	0.019	0.2487	64	10	47.9	28.1	105.0	76.0	1.38
10RD	4400	8.75	20.5	143.5	0.019	0.16	64	10	27.7	22.2	91.0	49.9	1.82
10TA	4800	10.0	20.5	205	0.018	0.400	64	10	69.6	31.4	141.5	101.0	1.40
10TC	5300	8.75	20.5	143.5	0.019	0.129	64	10	22.2	24.8	105.0	47.0	2.23
10TD	5300	8.75	20.5	143.5	0.019	0.000	64	10	0.0	26.0	132.5	26.0	5.10
10ITA	4400	10.0	21.5	215	0.019	0.400	64	10	72.0	29.0	135.0	101.0	1.34
10ITC	4800	8.75	21.5	150.5	0.018	0.321	64	10	50.9	22.2	128.5	73.1	1.76
10ITD	4750	8.75	21.5	150.5	0.018	0.123	64	10	22.6	25.4	79.0	48.0	1.65
12RA	4400	10.0	20.5	205	0.019	0.400	64	12	61.0	28.0	110.0	89.0	1.24
12RD	4200	9.0	20.5	143.5	0.019	0.118	64	12	32.3	30.6	99.5	62.9	1.58

## Response 2000™

The beam specimens were analyzed with a specialty computer program called Response 2000™. The program was developed by E. Bentz at the University of Toronto (Bentz, 2000). The program uses a sectional analysis approach to assess the load-deformation response of cross-sections subject to bending moments, shear forces, and axial loads. Constitutive relationships between stresses and strains at a section are based on Modified Compression Field Theory. The program accommodates many different cross-sectional shapes, is easy to use, and is available free from <http://www.ecf.utoronto.ca/~bentz/r2k.htm>. The program predicts the shear-moment failure surface for a specified cross-section, although the V-M response for high shear to moment ratios is not well predicted. Additionally, the program computes the AASHTO nominal V-M capacity curve based on MCFT for a specified cross-section.

Corrosion damage was incorporated by changing the effective beam web width and considering average area or minimum area due to section-loss of the stirrups. The results of Response 2000™ shear capacity prediction are shown in Table C9. Example shear force-midspan deflection responses for select specimens are shown in Figs. C5 and C6. The prediction of shear capacity for corrosion damaged specimens could be significantly different, depending on the rebar area chosen in the model. This difference is best illustrated for specimen 10RD shown in Figure C6. Average and local maximum cross-sectional loss were 26% and 60.5%, respectively for this specimen and the impact on the model prediction is large. However, the response of the specimen prior to significant nonlinearity was similar for both approaches. Prediction of shear capacity using the average stirrup section-loss are shown in Table C9 and Figure C7a. The Response 2000 analysis using average stirrup area provided  $V_{\text{EXPERIMENT}}/V_{\text{RESPONSE}} = 1.08$  and a coefficient of variation of 0.11. The analysis using local minimum area tended to under-estimate shear capacity and had larger scatter as shown in Table C8 and Figure C7b. Using the minimum stirrup area, resulted in a mean value for the  $V_{\text{EXPERIMENT}}/V_{\text{RESPONSE}} = 1.50$  and a coefficient of variation of 0.55.

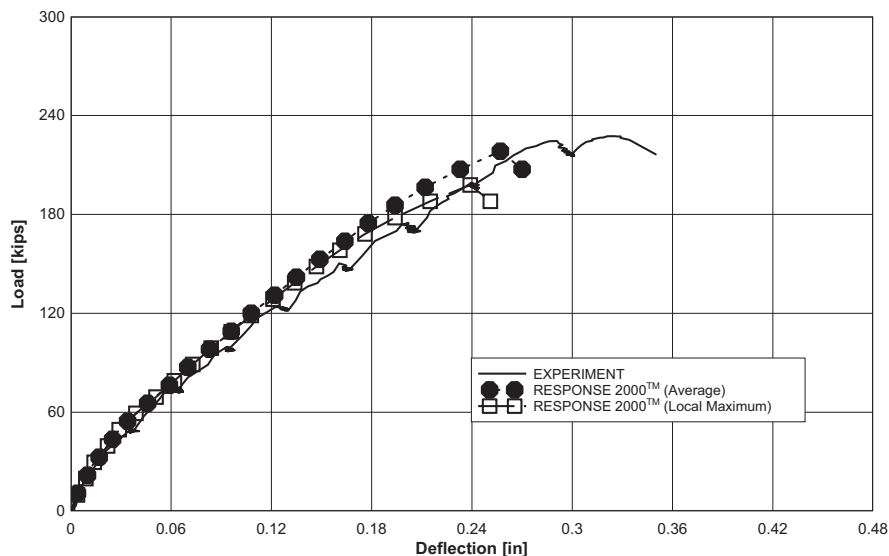


Figure C5: Experimental and analytical prediction of shear capacity from Response 2000, specimen 10RB

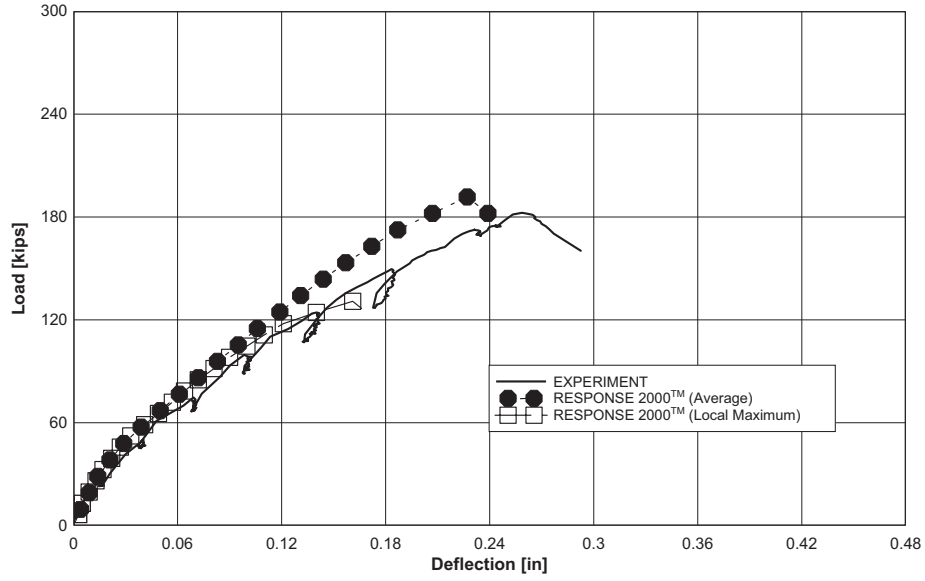


Figure C6: Experimental and analytical prediction of shear capacity from Response 2000, specimen 10RD

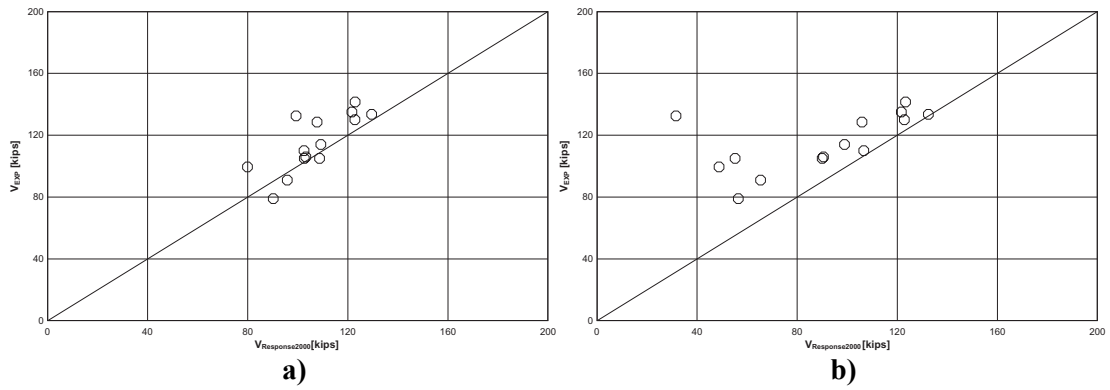


Figure C7: Experimental and analytical prediction of shear capacity from Response 2000

**Table C9: RESPONSE 2000™ results using proposed corrosion damage model**

Beam	f <sub>c</sub> [psi]	b <sub>e</sub> [in]	A <sub>v</sub> (leg) [in <sup>2</sup> ]		V <sub>RESPONSE</sub> [kips]		V <sub>EXP</sub> [kips]	V <sub>EXP</sub> /V <sub>RESPONSE</sub>	
			Average	Local Max	Average	Local Max		Average	Local Max
8RA	4350	10	0.20	0.20	129.5	129.5	133.5	1.03	1.03
8RD	4150	8.5	0.142	0.111	103.2	90.5	106.0	1.03	1.17
10RA	4950	10	0.20	0.20	122.8	122.8	130.0	1.06	1.06
10RB	5000	8.75	0.174	0.145	109.2	98.9	114.0	1.04	1.15
10RC	5100	8.75	0.154	0.124	102.6	90	105.0	1.02	1.17
10RD	4400	8.75	0.148	0.080	95.8	65.4	91.0	0.95	1.39
10TA	4800	10	0.20	0.20	122.9	122.9	141.5	1.15	1.15
10TC	5300	8.75	0.160	0.065	108.7	55.2	105.0	0.97	1.90
10TD	5300	8.75	0.135	0.000	99.3	31.6	132.5	1.33	4.19
10ITA	4400	10	0.20	0.20	121.6	121.6	135.0	1.11	1.11
10ITC	4800	8.75	0.165	0.160	107.7	105.9	128.5	1.19	1.21
10ITD	4750	8.75	0.128	0.062	90.2	56.5	79.0	0.88	1.40
12RA	4400	10	0.20	0.20	102.5	102.5	110.0	1.07	1.07
12RD	4200	9	0.133	0.059	79.9	48.8	99.5	1.25	2.04

## Conclusions

Several analysis methods were used to predict the shear capacity of the damaged and undamaged test beams. The methods were modified to account for the corrosion induced damage to both the concrete section and stirrups. Based on results of the analyses, the following conclusions are presented:

1. Each of the methods considered could provide reasonable shear capacity prediction.
2. Modeling stirrup corrosion damage using average rebar section-loss in combination with the concrete damage model developed in the main report provided the best correlation with the experimental results. The average stirrup area is applied at the specified stirrup spacing.
3. Partial bonding between the concrete and stirrups may have prevented locally reduced cross-sectional areas from controlling the behavior of the specimens. In the field, cover spalling may be greater than that observed in the laboratory tests, and thus stirrups in service may fail at locally reduced cross-sections without transferring significant bond stresses.
4. Use of the minimum stirrup area would provide a conservative estimate of the shear capacity for each of the methods.

5. For girders with sequential stirrups that are completely corroded, analysts should consider using the average rebar area at wider spacing than shown in the structural drawings to reflect sequential discontinuous stirrup legs. The lower shear capacity from this alternative or the normal proposed approach should be used.
6. The program Response 2000 provided not only capacity, but also load-deformation response. While the displacements were not as well predicted as strength using this method, results provided an indication of the relative deformation capacity. Further, the program allows quick computation of different parameters as well as the AASHTO MCFT shear-moment interaction capacity.